



<b>Publication Year</b>	2015
<b>Acceptance in OA @INAF</b>	2020-04-24T16:19:18Z
<b>Title</b>	A Method to Search for Bulk Motions in the ICM with Chandra CCD Spectra: Application to the Bullet Cluster
<b>Authors</b>	LIU, ANG; Yu, Heng; TOZZI, Paolo; Zhu, Zong-Hong
<b>DOI</b>	10.1088/0004-637X/809/1/27
<b>Handle</b>	<a href="http://hdl.handle.net/20.500.12386/24231">http://hdl.handle.net/20.500.12386/24231</a>
<b>Journal</b>	THE ASTROPHYSICAL JOURNAL
<b>Number</b>	809

# A METHOD TO SEARCH FOR BULK MOTIONS IN THE ICM WITH *CHANDRA* CCD SPECTRA: APPLICATION TO THE BULLET CLUSTER

ANG LIU<sup>1</sup>, HENG YU<sup>1,2,3</sup>, PAOLO TOZZI<sup>1,4</sup>, AND ZONG-HONG ZHU<sup>1</sup>

<sup>1</sup>Department of Astronomy, Beijing Normal University, Beijing, 100875 China

<sup>2</sup>Dipartimento di Fisica, Università di Torino, Via P. Giuria 1, I-10125 Torino, Italy

<sup>3</sup>Istituto Nazionale di Fisica Nucleare (INFN), Sezione di Torino, Via P. Giuria 1, I-10125 Torino, Italy

<sup>4</sup>INAF—Osservatorio Astrofisico di Arcetri, Largo E. Fermi, I-50122 Firenze, Italy

Received 2015 April 23; accepted 2015 July 3; published 2015 August 5

## ABSTRACT

We propose a strategy to search for bulk motions in the intracluster medium (ICM) of merging clusters based on *Chandra* CCD data. Our goal is to derive robust measurements of the average redshift of projected ICM regions obtained from the centroid of the  $K_\alpha$  line emission. We thoroughly explore the effect of the unknown temperature structure along the line of sight to accurately evaluate the systematic uncertainties on the ICM redshift. We apply our method to the “Bullet cluster” (1E 0657-56). We directly identify 23 independent regions on the basis of the surface brightness contours, and measure the redshift of the ICM averaged along the line of sight in each. We find that the redshift distribution across these regions is marginally inconsistent with the null hypothesis of a constant redshift or no bulk motion in the ICM, at a confidence level of about  $2\sigma$ . We tentatively identify the regions most likely affected by bulk motions and find a maximum velocity gradient of about  $(46 \pm 13) \text{ km s}^{-1} \text{ kpc}^{-1}$  along the line of sight on a scale of  $\sim 260$  kpc along the path of the “bullet.” We interpret this as the possible signature of a significant mass of ICM pushed away along a direction perpendicular to the merging. This preliminary result is promising for a systematic search for bulk motions in bright, moderate-redshift clusters based on spatially resolved spectral analysis of *Chandra* CCD data.

**Key words:** galaxies: clusters: individual (1E 0657-56) – galaxies: clusters: intracluster medium – X-rays: galaxies: clusters

## 1. INTRODUCTION

X-ray spectral diagnostics of galaxy clusters is a very powerful tool for characterizing the properties of the intracluster medium (ICM). In addition to density, temperature, and metal abundance of the diffuse baryons, another piece of information is the velocity derived from the Doppler shift of the spectral lines emitted by heavily ionized elements. ICM velocity is a critical diagnostic to investigate the dynamics of the cluster and its evolution. In particular, bulk motions and turbulence are expected as a consequence of major merger events. The majority of the merger events occurring during the lifetime of a galaxy cluster can produce gas motion at the level of  $100 \text{ km s}^{-1}$  (Nagai et al. 2013). However, major, off-center merger events are rare but may provide significant angular momentum to the ICM associated with bulk velocities of several thousand  $\text{km s}^{-1}$ .

The ubiquitous  $K$ -shell line complex of the H-like and He-like iron in the 6.7–6.9 keV rest frame, originally detected by Mitchell et al. (1976), is the most prominent feature in the X-ray spectra of massive clusters. Many other emission lines, including the  $L$ -shell from iron and  $\alpha$  element transitions, may be found particularly in the soft energy range (0.5–2.0 keV). However, considering that clusters are now detected in the X-ray up to redshift  $z \sim 1.75$  (see Brodwin et al. 2015), the  $K_\alpha$  iron complex is the only one which is potentially detectable in the ICM at any redshift with a total number of net counts as low as  $\sim 1000$  in the entire X-ray band. Indeed, the 6.7–6.9 keV emission-line complex has been identified in the large majority of clusters observed in X-ray at  $z \leq 1.5$  (Rosati et al. 2004, 2009; Stanford et al. 2005; Tozzi et al. 2013), while this appears to be challenging at  $z > 1.5$  (see, e.g., Tozzi et al. 2015).

Needless to say, the identification of iron line emission is crucial for measuring the redshift of newly discovered clusters in X-ray surveys. Yu et al. (2011) searched for the  $K_\alpha$ -shell iron emission lines with blind X-ray spectroscopy in 46 *Chandra* clusters in order to investigate the reliability of the measurement of X-ray redshift in medium- and high- $z$  clusters. The goal was to find the data quality requirements necessary to achieve robust redshift measurements in future X-ray cluster surveys. Recently, Tozzi et al. (2014) applied this technique to measure the redshift of a few newly discovered clusters in the Swift X-ray Cluster Survey (Tundo et al. 2012; Liu et al. 2015).

As already mentioned, the Doppler shift of the  $K_\alpha$ -shell emission lines of iron also offers a direct means of investigating the dynamics of the ICM along the line of sight through spatially resolved X-ray spectroscopy. Despite this interesting possibility, the iron line complex has rarely been used to search for bulk motions in the ICM. The main reason behind this is that the spectral resolution of CCD spectra at the relevant energies is too low compared to the expected effects. In the case of *Chandra*, the FWHM is  $\sim 285$  and  $\sim 150$  eV in ACIS-I and ACIS-S, respectively, at 5.9 keV.<sup>5</sup> Considering only low-redshift clusters with  $z \leq 0.3$ , the resolving power in the observing frame around the iron line complex is in the range 18–24 and 35–46 in ACIS-I and ACIS-S, respectively. This allows one to measure velocity differences of the order of at least a few thousand  $\text{km s}^{-1}$ , which may occur only in major mergers. On the other hand, grating data with much higher spectral resolution power, of the order of  $\sim 1000$ , can only probe the soft band, and will only have angular resolution in

<sup>5</sup> <http://cxc.harvard.edu/proposer/POG/html/chap6.html>

the cross-dispersion direction, making it difficult to identify regions with different motions.

Despite these difficulties, CCD data has the advantage of providing spatially resolved spectral analysis, which is crucial to unambiguously separate ICM regions with different velocities. A few cases of successful measurements of bulk motions in the ICM with CCD data have been reported in the literature. A first attempt concerned the Centaurus cluster, where bulk motions in the ICM were found in the spatially resolved spectral analysis of *ASCA* (Dupke & Bregman 2001a) and, eventually, *Chandra* data (Dupke & Bregman 2006), for a velocity difference of  $(2.4 \pm 0.1) \times 10^3 \text{ km s}^{-1}$  (but see also Ota et al. 2007). Signs of bulk motions were also found by *ASCA* in the Perseus cluster (Dupke & Bregman 2001b). A systematic search with *ASCA* found reliable signatures of bulk motions in the ICM in 2 out of 12 low-redshift ( $z < 0.13$ ) clusters (Dupke & Bregman 2005). A significant difference in velocity of  $(5.9 \pm 1.6) \times 10^3 \text{ km s}^{-1}$  between two regions of Abell 576 has been found by combining *Chandra* and *XMM-Newton* data (Dupke et al. 2007). Other clusters have been simply reported to show a significant discrepancy between the average redshift of the ICM and that of the BCG, as in the case of Abell 85 observed with *XMM-Newton* (Durret et al. 2005). This can be interpreted as a signature of different dynamics between the collisionless stellar component and the ICM, and it does not represent a measurement of bulk motions within the ICM.

A few single clusters were studied in detail with *Suzaku* thanks to the spectral resolution of the X-ray Imaging Spectrometer, which is comparable to *Chandra* ACIS-I. However, *Suzaku* has a better sensitivity to the  $K_\alpha$  iron emission-line complex than *Chandra* and *XMM-Newton* thanks to its lower background. Only upper limits of the order of  $2000 \text{ km s}^{-1}$  are derived for AWM7, Abell 2319, and Coma (Sato et al. 2008; Sugawara et al. 2009; Sato et al. 2011, respectively), or of  $\sim 300 \text{ km s}^{-1}$  for the Centaurus cluster (Tamura et al. 2014b). Only in one case (Abell 2256, Tamura et al. 2011) has a robust detection of a bulk motion of  $1500 \pm 300 \text{ km s}^{-1}$  been found. In this case, the redshift difference is consistent with that measured from optical spectroscopy between two subgroups of member galaxies, and therefore the ICM is found to be moving together with galaxies as a substructure within the cluster. To summarize, very few cases of bulk motions in the ICM have been successfully detected so far, and most of these have been due to the relative motions of different massive halos not yet merged and still carrying their ICM, as opposed to bulk motions occurring within the ICM of a single virialized halo.

Among the best-studied major mergers, 1E 0657-56 (the so-called ‘‘Bullet cluster’’) occupies a special place thanks to the extensive investigations in the last 10 years devoted to its dynamical structure. X-ray observations of *ASCA* and *ROSAT* showed a very high ICM temperature of  $\sim 17 \text{ keV}$  and a double peaked X-ray surface brightness distribution (Tucker et al. 1998). Using more accurate observations from *Chandra*, Markevitch et al. (2002) obtained a lower temperature of  $\sim 14.8 \text{ keV}$ . A viable explanation for such a high temperature is a recent, supersonic merging of two components. One of these components, called the ‘‘bullet,’’ has already crossed the main cluster and formed a bow shock, which is clearly visible in the X-ray image. The temperature map of 1E 0657-56 is shown to be consistent with this picture (Million & Allen 2009). Optical

observations showed that the spatial distribution of the cluster’s member galaxies was offset from the X-ray emission of the ICM (Barrena et al. 2002), and the gravitational potential, reconstructed with gravitational lensing, is also displaced with respect to the X-ray emission. On the other hand, the gravitational potential is spatially consistent with the distribution of the member galaxies, as expected if the potential well is dominated by a collisionless dark matter component (Clowe et al. 2004, 2006). This observation has been considered as a direct confirmation of the existence of dark matter (Bradač et al. 2006; Angus et al. 2007; Clowe et al. 2007). The discontinuity in the gas density and temperature across the shock can be used to estimate the velocity of the bullet perpendicularly to the line of sight (Markevitch et al. 2004). The Mach number of the bow shock was constrained to be  $M = 3.0 \pm 0.4$ , which corresponds to a tangential shock velocity of  $\sim 4700 \text{ km s}^{-1}$  (Markevitch et al. 2006; Markevitch & Vikhlinin 2007). The radial component of the velocity was determined to be  $\sim 600 \text{ km s}^{-1}$  based on the optical spectroscopic redshifts of member galaxies (Barrena et al. 2002). Since this value is much lower than the tangential component, the direction of the bullet is expected to be almost perpendicular to the line of sight.

Although the velocity difference along the line of sight between the two dark matter halos involved in the merger is expected to be modest (compared to the typical CCD resolution), we argue that the violent merger may have pushed a significant amount of ICM perpendicular to the direction of the merger, possibly resulting in significant bulk motions along the line of sight. In fact, we do not expect to measure in the ICM the same velocity value of the infalling clump, but instead the induced bulk motions which eventually will dissipate the coherent kinetic energy of the impact into thermal energy and turbulence in the ICM. Therefore, in this work, we intend to exploit the exquisite angular resolution of the *Chandra* satellite to perform spatially resolved spectral analysis in several different regions to investigate the presence of bulk motions in the ICM of the Bullet cluster. *Chandra* is also ideal to perform this study thanks to its robust calibration and its well-understood background.

The paper is organized as follows. In Section 2, we describe the strategy employed to search for bulk motions in the ICM. In Section 3, we describe a series of spectral simulations used to support our adopted analysis strategy. In Section 4, we describe the X-ray data reduction and analysis for the entire set of observations of the Bullet cluster, and finally provide a distribution of X-ray redshift associated with  $\sim 23$  independent regions of its ICM. We will provide an accurate evaluation of the errors on each redshift measurement with a particular emphasis on the treatment of systematics associated with the unknown temperature structure of the ICM. In Section 5, we investigate the distribution of the redshift of the ICM across the Bullet cluster to infer the presence of bulk motions and discuss our results in the context of the global dynamics of the Bullet cluster. In Section 6, we evaluate a posteriori the effect of uncertainties in the gain calibration of *Chandra* ACIS-I through the measurement of the position of two prominent fluorescence lines in the background. In Section 7, we discuss the possible extension of this work and future perspectives for the detection of bulk motions in the ICM with present and future X-ray facilities. Finally, in Section 8, we summarize our results. Throughout this paper, we adopt the 7 year *WMAP* cosmology

with  $\Omega_m = 0.272$ ,  $\Omega_\Lambda = 0.728$  and  $H_0 = 70.4 \text{ km s}^{-1} \text{ Mpc}^{-1}$  (Komatsu et al. 2011). Quoted error bars always correspond to  $1\sigma$  confidence levels.

## 2. A METHOD TO SEARCH FOR BULK MOTIONS IN THE ICM

Our method to search for bulk motions in the ICM is a two-step process. The first step consists of identifying the projected regions where the average X-ray redshift will be measured. This step must be kept as simple as possible to avoid the introduction of bias in the redshift measurements. In fact, the ab initio use of spectral information, such as identifying regions on the basis of their hardness ratio, may lead to the selection of regions with maximally different spectra, which can, in turn, amplify the redshift differences in a non-trivial way. For these reasons, we will choose the independent regions to be analyzed only on the basis of the surface brightness contours, after setting an appropriate requirement on the minimum signal-to-noise ratio (S/N) in each region.

The second step is to perform a standard spectral analysis to measure simultaneously the ICM temperature, heavy element abundances, X-ray redshift, and corresponding errors in the selected regions. This step is critical because of the unknown temperature structure of the ICM along the line of sight. We know that a significant range of temperatures is likely to be present in all of our spectra. We also know that the high temperatures involved make it impossible to constrain the different thermal components, or, in other words, the emission measure of the ICM as a function of the temperature. The main reason is that for temperatures above 3–4 keV, any mix of different temperatures is fit with a very good approximation by a single-temperature thermal emission model (Mazzotta et al. 2004). Nevertheless, the centroid of the iron line complex depends significantly on the mix of temperatures involved. To properly take this effect into account, we choose to describe our spectra always as a combination of two thermal components with different temperatures. Eventually, to include the effects of any possible mix of different temperatures in the ICM, we will consider any combination of temperature pairs allowed by the data to evaluate the maximum variation in the X-ray redshift associated with the underlying temperature distribution. This step allows us to fully include the effects of the ICM thermal structure without resorting to complex multi-temperature models, and directly provides a conservative estimate of the systematic uncertainty on the measured X-ray redshift. This systematic error will be added independently to the statistical error. The details of this step will be given in Section 4.3.

Another relevant aspect is the choice to limit our spectral analysis to the hard (2.0–10 keV) band. The main reason for this is that we prefer to base our result uniquely on the centroid of the iron line emission complex in the 6.7–6.9 keV rest frame. In principle, the inclusion of the soft 0.5–2.0 keV band offers the possibility to measure additional *L*-shell lines from iron and other elements, and to obtain a better measurement of the continuum, which is also useful to accurately measure the line positions. However, the inclusion of the soft band makes the X-ray fit much more complicated due to the possible presence of small amounts of much colder gas with potentially different dynamical status contributing *L*-shell lines. Therefore, the choice of the hard band is preferred since it would minimize the impact of systematics associated with complex dynamical and thermodynamical structures. Clearly, the consequence is larger

statistical errors with respect to the case of a full band analysis. As we will show with simulations, this effect is not large in the case of the Bullet cluster since the emission is dominated by very hot gas, whose emission lines in the soft band have a negligible contribution. In addition, the continuum in the soft band is strongly dependent on the value assumed to describe the Galactic absorption. In turn, Galactic absorption has a negligible impact in the hard band. Therefore, limiting our spectral analysis to the hard band only allows us to avoid another source of systematic uncertainties. Nevertheless, we still allow for a range of values in the Galactic hydrogen column density  $N_{\text{H}}$ .

To summarize, the spectra are fit with *Xspec* v12.8.2 (Arnaud 1996). To model the X-ray emission, we use two *mekal* plasma emission models (Mewe et al. 1985, 1986; Kaastra 1992; Liedahl et al. 1995), which include thermal bremsstrahlung and line emission with abundances measured relative to the solar values of Asplund et al. (2005) in which  $\text{Fe}/\text{H} = 3.6 \times 10^{-5}$ . We note that Million & Allen (2009) found evidence for a power-law component in some regions of the Bullet cluster, possibly associated with Inverse Compton on the CMB photons through a relativistic population of electrons. We do not attempt to model such non-thermal emission and argue that this component, if present, would be accounted for by a high-temperature, low-metallicity component, and therefore its effect would automatically be included in our estimate of the total error. Galactic absorption is described by the model *tbabs* (Wilms et al. 2000). The central value for the Galactic HI column density is set to  $N_{\text{HGal}} = 4.88 \times 10^{20} \text{ cm}^{-2}$  based on Kalberla et al. (2005). In Million & Allen (2009), the value of  $N_{\text{HGal}}$  at the position of the Bullet cluster has been measured from the X-ray analysis to be 4.44 or  $4.99 \times 10^{20} \text{ cm}^{-2}$ , depending on the fitting model, with a  $1\sigma$  error bar of 3%. We choose to allow  $N_{\text{HGal}}$  to vary by an interval of  $2\sigma$  ( $\sim 6\%$ ) around the value of Kalberla et al. (2005). During the minimization procedure, the redshift parameters of both thermal components are linked together, while the two temperatures and the two abundances are left free. We apply Cash statistics (Cash 1979) to the unbinned source plus background spectra in order to exploit the full spectral resolution of the ACIS-I instrument. Cash statistics is preferred with respect to the canonical  $\chi^2$  analysis of binned data, particularly for faint spectra (Nousek & Shue 1989). Since it is important for us to avoid local minima in the fitting procedure, the fit is repeated several times before and after running the command *steppar* on all of the free parameters, particularly the redshift, with a step of  $\delta z = 10^{-4}$ . Finally, the plots of  $\Delta C_{\text{stat}}$  versus redshift are visually inspected to investigate whether there are other possible minima around the best-fit values (see Yu et al. 2011).

## 3. SPECTRAL SIMULATIONS

We run a set of spectral simulations to provide support to the analysis strategy outlined in Section 2 and to investigate our ability to recover the correct input redshift with this strategy. As already mentioned, the most relevant aspect we want to tackle when measuring the X-ray redshift is the presence of a multi-temperature structure along the line of sight. The main point is the dependence of the centroid of the iron line complex on the mix of temperatures present in the ICM. In general, we will not be able to resolve the thermal structure of the ICM,

particularly at the high temperatures which are often found in massive, merging clusters.

To investigate this aspect, we perform a first series of simulations of spectra modeled with three thermal components. Typically, we choose two components with high temperatures ( $>5$  keV) and comparable emission measures, and a colder component ( $\sim 3.5$  keV) with an emission measure equal to 10% of that of the hotter components. The redshift is  $z_{\text{input}} = 0.30$  and  $\text{NH}_{\text{Gal}} = 4.89 \times 10^{22} \text{ cm}^{-2}$  for all of the components. Typical abundances are set to solar and half solar for the cold and hot components, respectively (in units of Asplund et al. 2005). The normalizations are set in order to have  $\sim 20,000$  net counts in the 0.5–10 keV band for an exposure of  $\sim 500$  ks to reproduce at best the typical situation of the actual data (see Section 4.1). Each set is simulated 10,000 times, and the background, RMF, and ARF files are taken from the real *Chandra* ACIS-I data to reproduce the instrumental set up we have for our spectra. As described in Section 2, in the spectra analysis, we link together the redshift of the thermal components while the temperatures, abundances, and normalizations are left free.

We are aware that the discrete distribution of the emission measure as a function of the temperature in the simulated spectra is not meant to provide a realistic description of the actual ICM thermal structure; nevertheless, it is representative of the situation often encountered in the ICM regions of the Bullet cluster, and therefore represents a useful testbed for our analysis strategy. In fact, it is very hard to propose a realistic, continuous distribution of emission measures in the Bullet cluster, an aspect which should be treated in its full complexity with hydrodynamical simulations.

There are three relevant choices in our strategy: the method to find the best-fit parameters, the energy band to be considered, and the fitting model. First, we set up the optimal method by running the standard analysis on our simulated spectra and comparing the results with those obtained with a simple one-step, direct fit. In our standard analysis, we repeat the fit several times after running the `steppar` command on the redshift parameter in an interval  $\pm 0.05$  around the input redshift of  $z_{\text{input}} = 0.3$  with a step of  $\delta z = 0.0001$ . This procedure avoids the local minima and it is able to find the global minima in most cases. We find that in many cases (at least 30%), the best-fit redshift obtained with a direct fit (i.e., running the `fit` command only once) provides incorrect results due to a local minimum far from the input redshift. On the other hand, with our procedure, the correct minimum is found in the large majority of the cases. Therefore, we do not discuss this aspect further, and henceforth adopt as the standard procedure the use of the `steppar` command with  $\delta z = 0.0001$  on the redshift parameter.

Next, we focus on the effect of using two `mekal` models instead of one when fitting the simulated spectra, and of considering only the 2.0–10 keV band instead of the entire 0.5–10 keV band. In Figure 1, we have an example of the effect of the energy band and of the adopted model, obtained with input parameters  $kT_1 = 8$  keV,  $kT_2 = 15$  keV, and  $Z_1 = 0.6 Z_{\odot}$  and  $Z_2 = 0.4 Z_{\odot}$ , plus a third thermal component with  $kT_3 = 3.5$  keV and  $Z_3 = 1.0 Z_{\odot}$ . We plot the distribution of the best-fit values of the X-ray redshift  $z_X$  obtained while fitting the simulated spectra with one (left panels) and two (right panels) thermal components, on the 0.5–10 keV (upper panels) and the 2.0–10 keV (lower panels) energy bands. We find that

in all of the cases, we are able to recover the input redshift with good accuracy. However, the use of the two-temperature `mekal` model provides average redshift values slightly closer to the input value, as shown in Table 1 where we summarize the results of this particular set of simulations. Despite being very small, this effect is found in all of our simulations, irrespective of the input temperatures and abundances. We also estimate the dispersion of the  $z_X$  distribution  $\sigma_{\text{rms}}^2 \equiv \sum_i (z_{X,i} - \langle z_X \rangle)^2 / (N - 1)$ . As expected, we find a larger  $\sigma_{\text{rms}}$  when using the two-temperature model due to the degeneracy between the temperature values that affect the redshift. This effect provides  $\sim 20\%$  larger errors in all of our simulations. On the other hand, we note that the uncertainties on the redshift found using the total and hard bands are comparable. This is due to the fact that we simulated high-temperature spectra, and therefore we typically have no relevant lines in the soft band which can add significant information. We conclude that the conservative choice of using a two-temperature `mekal` model on the hard 2.0–10 keV provides robust and accurate results.

We now use our simulations to investigate the accuracy of the statistical error provided by *Xspec* compared to the actual dispersion of the distribution of the best-fit  $z_X$ . We run another set of simulations and analyze them directly with a two-temperature thermal model. Each simulation set includes  $10^3$  spectra with an average of  $2 \times 10^4$  net counts as observed in an exposure of 500 ks with ACIS-I, with an input model provided by two `mekal` components with the same emission measure. The input parameters for the temperatures and abundances are shown in Table 2. The input redshift is always  $z_{\text{input}} = 0.3$ . This grid has been chosen in order to represent the values expected in the complex temperature structure of the Bullet cluster (see Million & Allen 2009). For each set of parameters, we obtain the distribution of best-fit values of  $z_X$  with our standard analysis procedure, which is shown in Figure 2. We also derive two additional pieces of information: the average  $1\sigma$  statistical error obtained with the *Xspec* command `'error 1.0,'` computed as  $\langle \sigma_{\text{stat}} \rangle \equiv \sum_i \sigma_{\text{stat},i} / N$ , where  $\sigma_{\text{stat},i}$  is simply the average of the lower and upper  $1\sigma$  error bars on  $z_X$  estimated in the  $i$ th simulated spectrum. Then, we also compute the rms dispersion of the histogram distribution as  $\sigma_{\text{rms}}^2 \equiv \sum_i (z_{X,i} - z_{\text{input}})^2 / N$ . By comparing  $\langle \sigma_{\text{stat}} \rangle$  and  $\sigma_{\text{rms}}$ , we are able to verify whether the statistical error is representative of the true uncertainty on  $z_X$ . In the last columns of Table 2, we show the values of  $\langle \sigma_{\text{stat}} \rangle$ ,  $\sigma_{\text{rms}}$ , and their ratio. In all of these cases, we note that  $\sigma_{\text{rms}}$  is larger than the direct estimate of the statistical error by 15%–35%. Therefore, we conclude that the actual uncertainty on the best-fit  $z_X$  is significantly larger than the estimated statistical error. This effect is due to the strong degeneracy between the parameters of the fitting model. This is confirmed by a broad, highly scattered correlation between the deviation of  $z_X$  with respect to the input value and the global deviation from the input temperatures that we observe in our simulations. We are also aware that the ratio  $\sigma_{\text{rms}} / \langle \sigma_{\text{stat}} \rangle$  in real clusters may be even larger than the values listed in Table 2, since the actual thermal structure of the ICM is expected to be more complex than a simple two-temperature thermal bremsstrahlung. One last point we can take away from Figure 2 is that the distribution of best-fit  $z_X$  is wider at larger temperatures. This simply reflects the difficulty in measuring the iron emission-line complex in high-temperature spectra.

Taken together, these results support our choice of measuring an additional systematic error associated with the

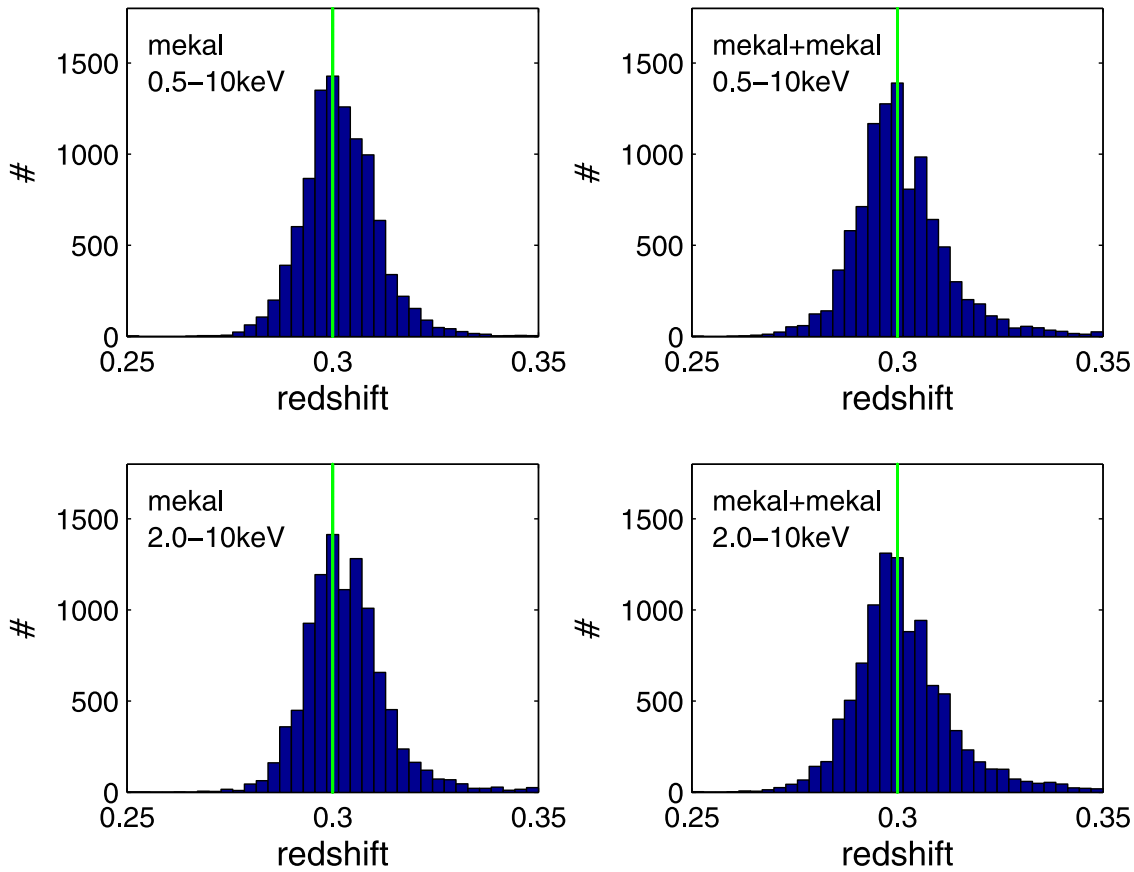


**Figure 1.** Upper left panel: distribution of the best-fit X-ray redshift  $z_X$  obtained fitting with a single-temperature `mekal` model a total of  $10^4$  spectra simulated assuming a two-temperature `mekal` model as an input with  $kT_1 = 8$  keV and  $kT_2 = 15$  keV,  $Z_1 = 0.6 Z_\odot$ ,  $Z_2 = 0.4 Z_\odot$ , and the same emission measure. A third component with  $kT_3 = 3.5$  keV and  $Z_3 = 1.0 Z_\odot$  has been added with a  $10\times$  lower emission measure. The redshift  $z_{\text{input}} = 0.30$  (shown as a vertical green line) is the same for both components. Simulated spectra have an average of  $2 \times 10^4$  net counts in the 0.5–10 keV band. Fits are performed over the entire energy range (0.5–10 keV). Upper right panel: same as the upper left panel, but using a two-temperature `mekal` model to fit the simulated spectra. Lower left panel: same as the upper left panel, but fitting only the hard band (2.0–10 keV). Lower right panel: same as the upper right panel, but fitting only the hard band (2.0–10 keV).

**Table 1**  
Results from the Simulations Shown in Figure 1

Model	Band (keV)	$\langle z_X \rangle$	$\sigma_{\text{rms}}$
mekal	0.5–10	0.3019	0.0092
mekal	2.0–10	0.3032	0.0099
2T mekal	0.5–10	0.3008	0.0113
2T mekal	2.0–10	0.3013	0.0119

**Note.** In column 3, we show the average value of  $z_X$ , while in column 4 we show the dispersion  $\sigma_{\text{rms}}$  of the best-fit  $z_X$  distribution.

**Table 2**  
Grid of Temperatures and Abundances Used as Input for the Simulations Shown in Figure 2

$kT_1$	$kT_2$	$Z_1/Z_\odot$	$Z_2/Z_\odot$	$\langle \sigma_{\text{stat}} \rangle$	$\sigma_{\text{rms}}$	$\sigma_{\text{rms}}/\langle \sigma_{\text{stat}} \rangle$
4.0	8.0	1.0	0.6	0.0029	0.0033	1.13
5.0	10.0	0.9	0.5	0.0037	0.0042	1.14
6.0	12.0	0.8	0.4	0.0048	0.0065	1.35
7.0	14.0	0.7	0.4	0.0061	0.0082	1.35
8.0	16.0	0.6	0.35	0.0078	0.0108	1.39
9.0	18.0	0.5	0.3	0.0105	0.0130	1.23

**Note.** In column five, we show the average statistical error on  $z_X$  directly obtained with *Xspec*, while in column six we show the dispersion  $\sigma_{\text{rms}}$  for the distribution of  $z_X$ . The ratio of these two quantities is shown in the last column.

unknown thermal structure of the ICM, as described in Section 2. To do that, for each region, we will derive the best-fit X-ray redshift for all of the possible combinations of temperatures and abundances sampled in a realistic range (from 3.5 to 27 keV and from 0.1 to  $1.6 Z_\odot$ , respectively) and measure the width of the distribution of the best-fit  $z_X(T_1, T_2, Z_1, Z_2)$ . This will provide us with the systematic uncertainty  $\sigma_{\text{sys}}$  on  $z_X$  associated with the unknown thermal composition of the ICM. The details of this step and the selection of a proper range of temperatures and abundances in each region will be described in full detail in Section 4.3. Finally, this uncertainty will be added to the statistical error to provide the total uncertainty  $\sigma_{\text{tot}}$  on the best-fit  $z_X$ .

## 4. X-RAY DATA REDUCTION AND ANALYSIS

### 4.1. Data Reduction

The *Chandra* observations used in this paper are listed in Table 3. We find 10 pointings of 1E 0657-56 in the *Chandra* archive, of which we choose 9 after discarding Obsid 554 which was taken in the FAINT mode. Due to the low exposure of Obsid 554 ( $\sim 26$  ks), this choice has little effect on our final results. The selected observations were carried out between 2002 July and 2004 August in VFaint mode using the ACIS-I. The data reduction is performed using the latest release

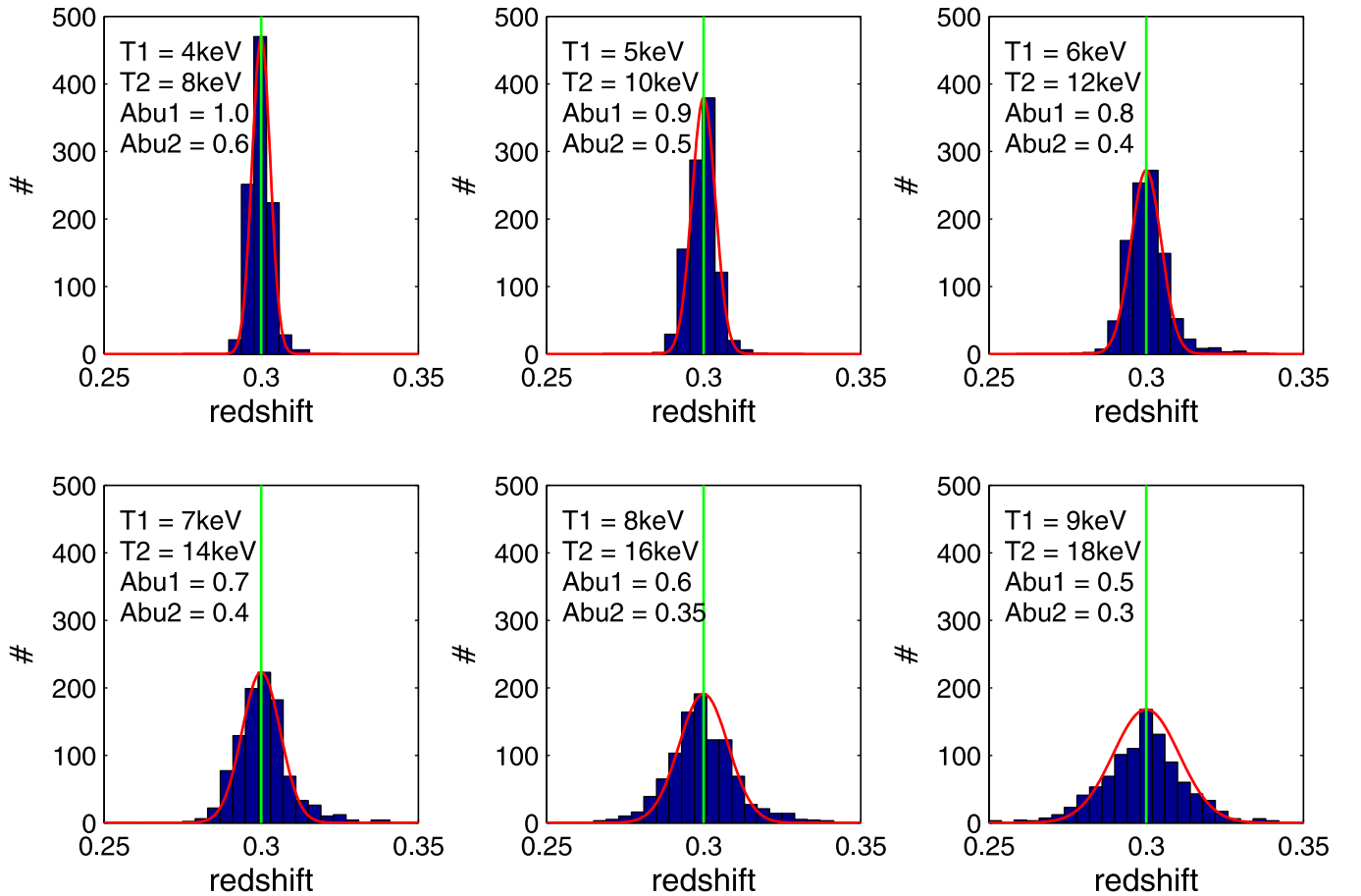


**Figure 2.** Histogram distribution of the best-fit redshift  $z_X$  for  $10^3$  simulated spectra with input temperature and abundances listed in Table 2 and  $z_{\text{input}} = 0.3$  (shown with a green vertical line). In red, we show the Gaussian with amplitude  $\sigma_{\text{rms}}$  centered on  $\langle z_X \rangle$ .

**Table 3**  
List of the Nine *Chandra* Observations Used in This Work

ObsID	Exposure (ks)	Observation Date
3184	87.4	2002 Jul 12
5355	27.4	2004 Aug 10
5356	97.1	2004 Aug 11
5357	79.0	2004 Aug 14
5358	32.0	2004 Aug 15
5361	82.6	2004 Aug 17
4984	76.1	2004 Aug 19
4985	27.4	2004 Aug 23
4986	41.4	2004 Aug 25

**Note.** All of the observations are taken in the VFAINT mode. In the second column, we list the effective exposure time after data reduction.

of the *ciao* software (version 4.6) with CALDB 4.6.7. Charge transfer inefficiency correction, time-dependent gain adjustment, grade correction, and pixel randomization are applied. We are able to filter efficiently the background events thanks to the VFAINT mode. This allows us to reduce the background by  $\sim 25\%$  in the hard (2.0–10 keV) band. Eventually, we search for high background intervals and remove them with a  $3\sigma$  clipping. The final exposure times of each Obsid, listed in Table 3, are lower than the nominal exposure time only by a few percent. The *level 2* event files obtained in this way are then reprojected to match the coordinates of Obsid 3184, and

merged to a single event file. The total exposure time of the merged data is  $\sim 550.4$  ks. The soft- (0.5–2.0 keV), hard- (2.0–10 keV), and total- (0.5–10 keV) band images are obtained from the merged file.

We select the regions from which we extract the spectra on the 0.5–10 keV band image. We apply the contour-binning technique of Sanders (2006), developed in order to select regions according to the surface brightness distribution of an extended source. Our goal is to obtain spectra with comparable constraints on the X-ray redshift. To do that, we ideally should require that there be a similar number of net counts in the 2.0–10 keV band in each region. However, since the range in region size is wide and we have a few regions with a much larger area than average (particularly in the outer part of the clusters), we prefer to set our criterion in terms of S/N in the total band. Therefore, in this way we select 23 regions with full-band S/N  $> 140$  each within a radius of  $104''$ , which is the circular region with the highest S/N in the 0.5–10 keV band, and will be used to compute the global redshift of the ICM (see Section 4.2).

In Table 4, we list the net counts measured in the soft and hard bands, and the S/N in the hard band, for the 23 regions defined by the contour-binning algorithm. We have at least  $\sim 7000$  net counts in each region in the 2.0–10 keV band with a maximum of 12,000/14,000 net counts for the largest regions. Note that this value is much larger than that generally used to measure temperature, iron abundance, and average X-ray redshift. Here, we set a higher threshold because we want to

**Table 4**  
Soft- and Hard-band Photometry of the 23 Regions  
Selected for Spectral Analysis

Region ID	Net Cts (0.5–2.0 keV)	Net Cts (2.0–10 keV)	S/N (2.0–10 keV)
0	13402 ± 116	6519 ± 82	78.8
1	12322 ± 111	7484 ± 88	84.1
2	12678 ± 113	7049 ± 86	81.1
3	12355 ± 112	7410 ± 88	83.4
4	20335 ± 149	12432 ± 133	93.3
5	12306 ± 111	7418 ± 89	83.1
6	12267 ± 111	7412 ± 89	82.8
7	12316 ± 112	7185 ± 88	80.8
8	12138 ± 111	7384 ± 89	82.1
9	12009 ± 110	7627 ± 91	83.5
10	12176 ± 111	7266 ± 90	80.6
11	15556 ± 129	9670 ± 113	85.2
12	12595 ± 115	7946 ± 99	79.7
13	12274 ± 112	7397 ± 90	81.6
14	11928 ± 111	7374 ± 91	80.6
15	11946 ± 110	7586 ± 91	82.8
16	11900 ± 111	7142 ± 91	78.0
17	20063 ± 144	12160 ± 120	100.8
18	21797 ± 153	14097 ± 136	103.4
19	11691 ± 110	7496 ± 93	80.0
20	11880 ± 111	7250 ± 92	78.1
21	12068 ± 111	7214 ± 90	79.5
22	11632 ± 109	7665 ± 92	82.5

**Note.** Errors on the net detected counts are computed as  $\sqrt{\text{Cts} + 2 \times B}$ , where Cts are the source Counts and  $B$  is the expected background Geometrically rescaled to the source Region.

achieve a precision on the X-ray redshift measurement larger than usually needed to evaluate global properties, and because of the exceptionally high temperatures in the ICM that make the iron emission-line complex less prominent. The discrete, color-coded surface brightness of the Bullet cluster, together with the shape of the selected regions, is shown in Figure 3.

Finally, we extract the spectra of each region in the full band. Thanks to the exquisite angular resolution of *Chandra*, we do not need to correct for effects due to the point-spread function when extracting the spectra. Before creating the spectra, we manually remove all of the point sources visible in the soft- and total-band images. For each region, we produce response matrix (RMF) and ancillary response (ARF) files from each Obsid, and then add the RMF and ARF files, weighing them by the corresponding exposure times. In this way, we keep track of all the differences in the ACIS-I effective area among different regions on the detector and among Obsid taken at different epochs. This is an important step, considering that the cluster is observed on different CCD (`ccd_id` = 3 for Obsid 3184, 4984, and 5361; `ccd_id` = 2 for Obsid 4985, 5355, and 5356; `ccd_id` = 0 for Obsid 4986, 5357, and 5358). The background is sampled from a series of circular regions as far as possible from the cluster emission, but still on the solid angle defined by the overlap of all the Obsid. In this way, we are not sampling regions where the exposure time is lower than 550 ks, and therefore the background can be simply geometrically scaled to the source region. The geometrical backscale values between the background region and the source region range from  $\sim 10$  to  $\sim 100$ , and the ratio of the background to the

ICM signal in the source region ranges from 2% up to 15% for the outermost region.

#### 4.2. Global ICM Redshift

As a first step, we measure the redshift of the ICM emission from the entire cluster, fitting the global spectrum in the 2.0–10 keV energy range. The extraction region of the global ICM emission is defined as the circle with the maximum S/N (see Yu et al. 2011) corresponding to a radius of 104". This circular region also provides the outer limit for the definition of the ICM regions, as shown in Figure 3.

Given the complex temperature structure encompassed by this large region, we find that one of the two temperatures hits the hard upper limit during the minimization procedure. Therefore, we freeze it to a reference maximum value of 26 keV. The best-fit X-ray redshifts obtained from the spectral analysis of the global emission from the cluster is  $z_{\text{Xglobal}} = 0.2999^{+0.0051}_{-0.0045}$ , obtained for two temperatures of 26 keV (frozen) and  $6.2^{+1.5}_{-1.3}$  keV, and iron abundances of  $(0.50 \pm 0.10) Z_{\odot}$  and  $0.40^{+0.16}_{-0.07} Z_{\odot}$  for the first and the second thermal components, respectively. We note that the best-fit value of the  $z_{\text{Xglobal}}$  is consistent within  $1 \sigma$  with the optical value  $z_{\text{opt}} = 0.296$ . We remark that we would obtain a value of  $0.3059 \pm 0.005$ , therefore, at  $\sim 2\sigma$  from the optical value if we had used a single `mekal` model instead of two. This is another hint toward the necessity of using at least two temperatures to properly model the thermal structure of the ICM, and therefore the shape of the iron line complex. We also note that the best-fit  $z_{\text{Xglobal}}$  is inconsistent with the value  $z = 0.325$  published in Yu et al. (2011). This is mostly due to the fact that in Yu et al. (2011), we used a one-temperature `mekal` model and adopted a much simpler minimization procedure. Our aim was to test the capability of recovering the X-ray redshift with a blind spectral analysis with a single-temperature `mekal` model, since this procedure was meant to be applied to a poorly characterized cluster. Therefore, the discrepancy found in Yu et al. (2011) is affected by the temperature structure of the ICM.

This result shows that the global ICM emission is dominated by gas which is moving along with those galaxies whose velocities lie mostly along the plane of the sky, with a small velocity component projected along the line of sight estimated to be  $\sim 600 \text{ km s}^{-1}$  based on optical spectroscopy (Barrena et al. 2002). This velocity component would correspond to a maximum difference between the galaxies and the majority of the ICM of  $\Delta z \sim 2.6 \times 10^{-3}$ , which is below the detection threshold of our analysis. As expected, the only means to detect any internal bulk motions induced by the merger is to restrict our analysis to small regions, exploiting the exquisite angular resolution of *Chandra* to search for regions where a relevant mass of gas has reached a velocity of at least  $\text{few} \times 1000 \text{ km s}^{-1}$  with respect to the bulk of the ICM.

#### 4.3. Spatially Resolved Spectral Analysis with Contour Binning

In this Section, we present the results from the fits of the 23 independent regions selected by the contour-binning technique. Fits are performed in the 2.0–10 keV energy range according to the strategy provided in Section 2. For each region, we produce a plot showing the  $\Delta C_{\text{stat}}$  value versus the redshift, obtained by varying the redshift parameter and marginalizing the fit with respect to the other parameters. Two examples are shown in

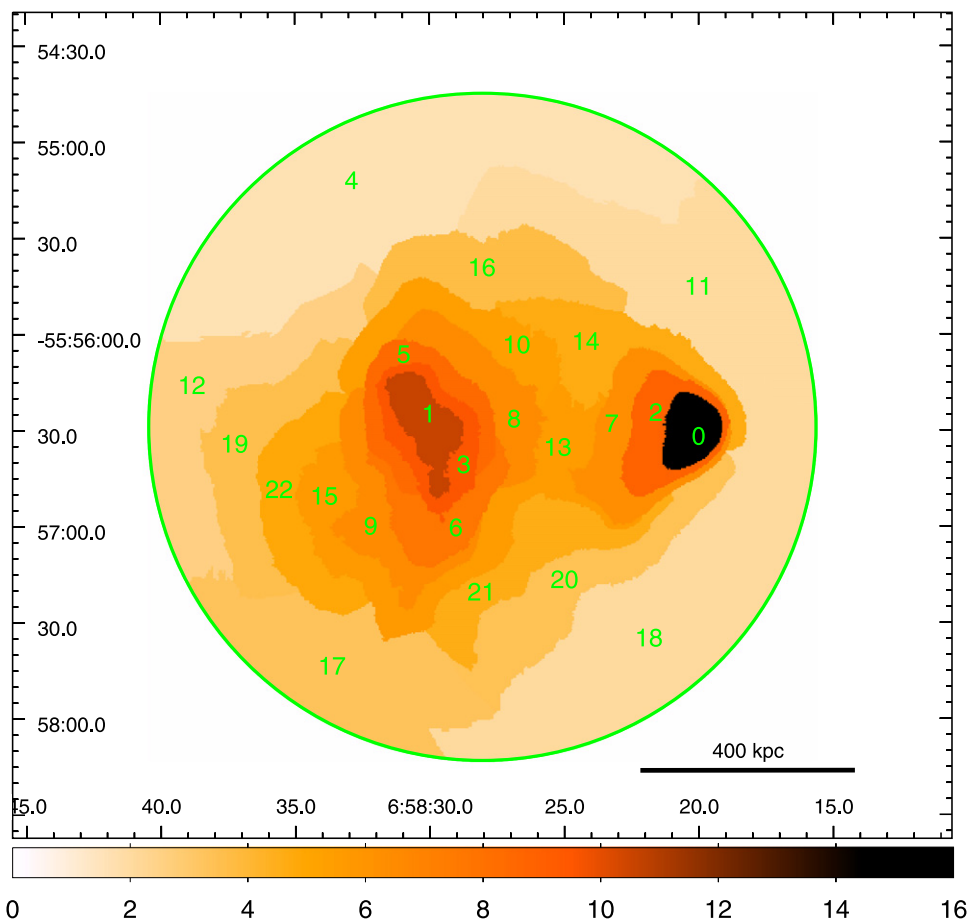


**Figure 3.** Color-coded surface brightness map of the Bullet clusters. Each of the 23 regions defined by the contour-binning technique are shown with a different color corresponding to the hard-band surface brightness. The units of the color bar are counts per pixel. The large circle shows the region used to extract the spectrum of the global cluster emission.

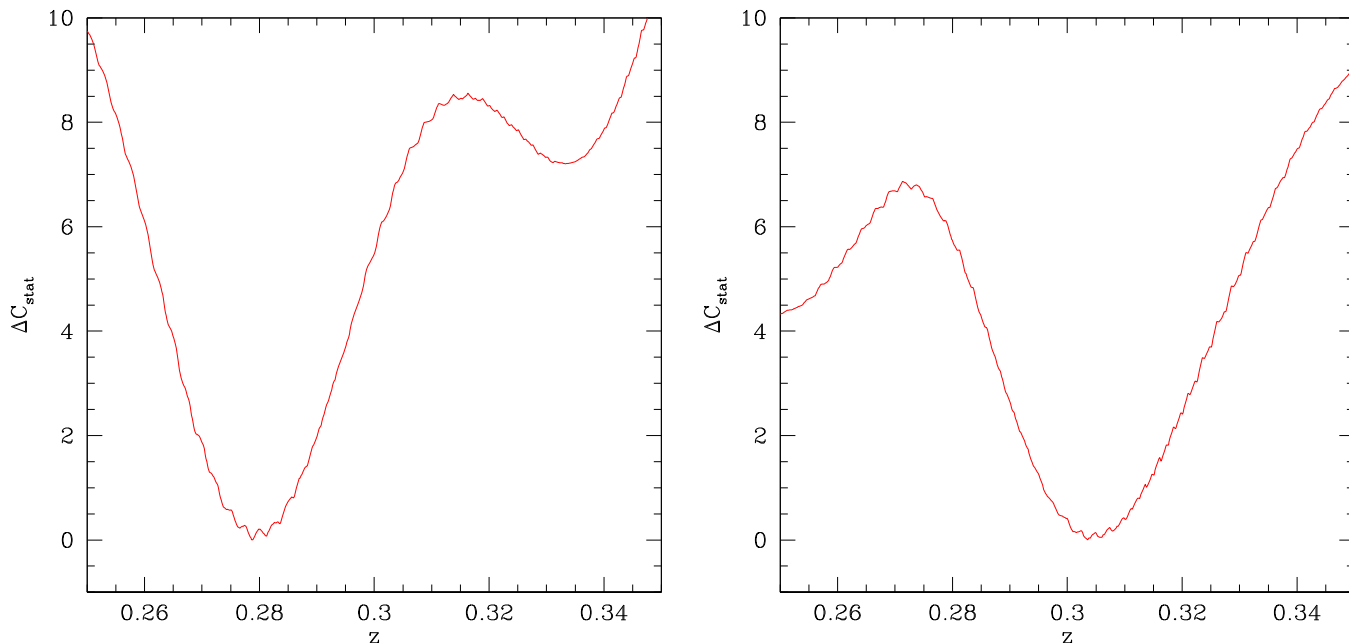


**Figure 4.** Plot of  $\Delta C_{\text{stat}}$  vs. redshift for region 4 (left panel) and region 9 (right panel).

Figure 4. The minimum is well defined and roughly symmetric, therefore providing a robust estimate of the statistical uncertainty. Nevertheless, we visually inspected all of the

$\Delta C_{\text{stat}}$  versus redshift plots, finding one anomaly in the case of regions 7 and 15, where two comparable minima are found. This may be due to the overlap of two comparable masses of

**Table 5**  
Results of the Spectral Fits of the ICM Projected Regions Shown in Figure 3

Region	$z$	$\sigma_{\text{stat}_b}$	$\sigma_{\text{stat}_u}$	$\sigma_{\text{syst}_b}$	$\sigma_{\text{syst}_u}$	$\sigma_{\text{tot}_b}$	$\sigma_{\text{tot}_u}$
0	0.3000	-0.0053	0.0047	-0.0025	0.0001	-0.0058	0.0047
1	0.3265	-0.0099	0.0090	-0.0050	0.0001	-0.0110	0.0090
2	0.2994	-0.0057	0.0027	-0.0001	0.0080	-0.0057	0.0084
3	0.2957	-0.0159	0.0201	-0.0001	0.0169	-0.0159	0.0262
4	0.2787	-0.0055	0.0081	-0.0001	0.0048	-0.0055	0.0094
5	0.2874	-0.0105	0.0087	-0.0029	0.0024	-0.0108	0.0090
6	0.2957	-0.0113	0.0105	-0.0047	0.0002	-0.0122	0.0105
7	0.2836	-0.0054	0.0088	-0.0001	0.0072	-0.0054	0.0113
8	0.2719	-0.0097	0.0067	-0.0032	0.0070	-0.0102	0.0096
9	0.3061	-0.0077	0.0108	-0.0026	0.0018	-0.0081	0.0109
10	0.3159	-0.0102	0.0092	-0.0056	0.0001	-0.0116	0.0092
11	0.3062	-0.0132	0.0122	-0.0027	0.0007	-0.0134	0.0122
12	0.3215	-0.0106	0.0095	-0.0087	0.0001	-0.0137	0.0095
13	0.3181	-0.0167	0.0137	-0.0099	0.0050	-0.0194	0.0145
14	0.2934	-0.0134	0.0302	-0.0026	0.0046	-0.0136	0.0305
15	0.3083	-0.0041	0.0085	-0.0038	0.0001	-0.0055	0.0085
16	0.2933	-0.0154	0.0187	-0.0023	0.0020	-0.0155	0.0188
17	0.3138	-0.0317	0.0181	-0.0179	0.0001	-0.0364	0.0181
18	0.3070	-0.0086	0.0084	-0.0056	0.0001	-0.0102	0.0084
19	0.2665	-0.0241	0.0175	-0.0071	0.0034	-0.0251	0.0178
20	0.2922	-0.0090	0.0134	-0.0001	0.0103	-0.0090	0.0169
21	0.2935	-0.0091	0.0104	-0.0001	0.0040	-0.0091	0.0111
22	0.2941	-0.0195	0.0191	-0.0006	0.0026	-0.0195	0.0192

**Note.**

Column 1: region number; column 2: best-fit redshift  $z_X$  obtained fitting the 2.0–10 keV energy range; columns 3 and 4: lower and upper  $1\sigma$  error bars from fit statistics; columns 5 and 6: lower and upper  $1\sigma$  error bars from systematics associated to the ICM temperature structure; columns 7 and 8: total lower and upper  $1\sigma$  error bars computed as  $\sigma_{\text{tot}} = \sqrt{\sigma_{\text{stat}}^2 + \sigma_{\text{syst}}^2}$

ICM with different redshift, but we cannot confirm this interpretation. We do not find similar cases in the remaining 21 regions. Therefore, we will exclude regions 7 and 15 when evaluating the probability of ICM bulk motions in Section 5.

In Table 5, we list the best-fit  $z_X$  with the corresponding lower and upper statistical error bars corresponding to the  $1\sigma$  confidence level. This list of values defines a redshift map of the ICM in the Bullet cluster, shown in Figure 5. The map appears to be patchy with the strongest redshift differences in the trail of the bullet, while there is no striking difference between the bullet and the surrounding gas, consistently with the finding that the merger is occurring in the plane of the sky. The  $z_X$  map suggests that significant bulk motions may be left behind the bullet's path, which eventually will evolve into turbulent motions.

The redshift map has also been derived using another background, chosen from an independent (not overlapping) region on the detector with the same characteristics as described in Section 4.1. We find minor differences which leave our results unaltered. We also repeated the fit with a synthetic background obtained from blank field *Chandra* data after normalizing it in the 2.0–10 keV band to our reference background extracted from the data. Again, we find consistency well within  $1\sigma$  for the best-fit parameters. Therefore, we conclude that our results are robust against variation in the background.

Before drawing any conclusion on any possible bulk motion of the ICM caused by the passage of the bullet, we need to carefully take into account the uncertainty on the velocity measurement in each region. However, as discussed in

Section 2 and shown with simulations in Section 3, the statistical errors may underestimate the actual uncertainties on the best-fit  $z_X$ , and therefore on the relative velocity  $v_{\text{ICM}} = c \times (z_i - \langle z_X \rangle) / (1 + \langle z_X \rangle)$ . Therefore, we need to evaluate in each region the uncertainty associated with the unknown thermal structure of the ICM along the line of sight.

To do so, we proceed as described in Section 3. We consider a four-dimensional grid of spectral parameters  $T_1$ ,  $T_2$ ,  $Z_1$ , and  $Z_2$  covering all of the possible values expected in the Bullet cluster. We set a lower limit of 3.5 keV and a maximum of 27 keV for the temperatures. As for the metal abundances, we make them range from 0.1 to 1.6 times the solar value (in units of Asplund et al. 2005). The steps of the grid are 0.5 keV for the temperature and 0.1 for the metal abundance. Clearly, this temperature and abundance grid is exceedingly wide for a single ICM region. Therefore, we selected a subgrid in the following way. First, for each region, we measure the best fit in the full (0.5–10 keV) band, leaving all of the parameters free, and collect the absolute minimum  $C_{\text{min}}$ . Then, we compute the best fit on the grid in the full (0.5–10 keV) band where only the redshift parameter and the two *mekal* normalizations are left free, while  $\text{NH}_{\text{Gal}}$  is allowed to vary in a 6% interval around the central value. Thus, we compute the best fit achievable for each set of values on the grid, and finally select all of the values whose best-fit  $C_{\text{stat}}$  is close enough to the absolute minimum  $C_{\text{min}}$ . The criterion we adopt is given by  $\Delta C_{\text{stat}} \equiv C_{\text{stat}} - C_{\text{min}} < 4.72$ , which corresponds to a  $1\sigma$  confidence level for four free parameters (see Press et al. 2002). In this way, we also exploit the information included in the soft band (0.5–2 keV). By applying the criterion  $\Delta C_{\text{stat}} < 4.72$  for

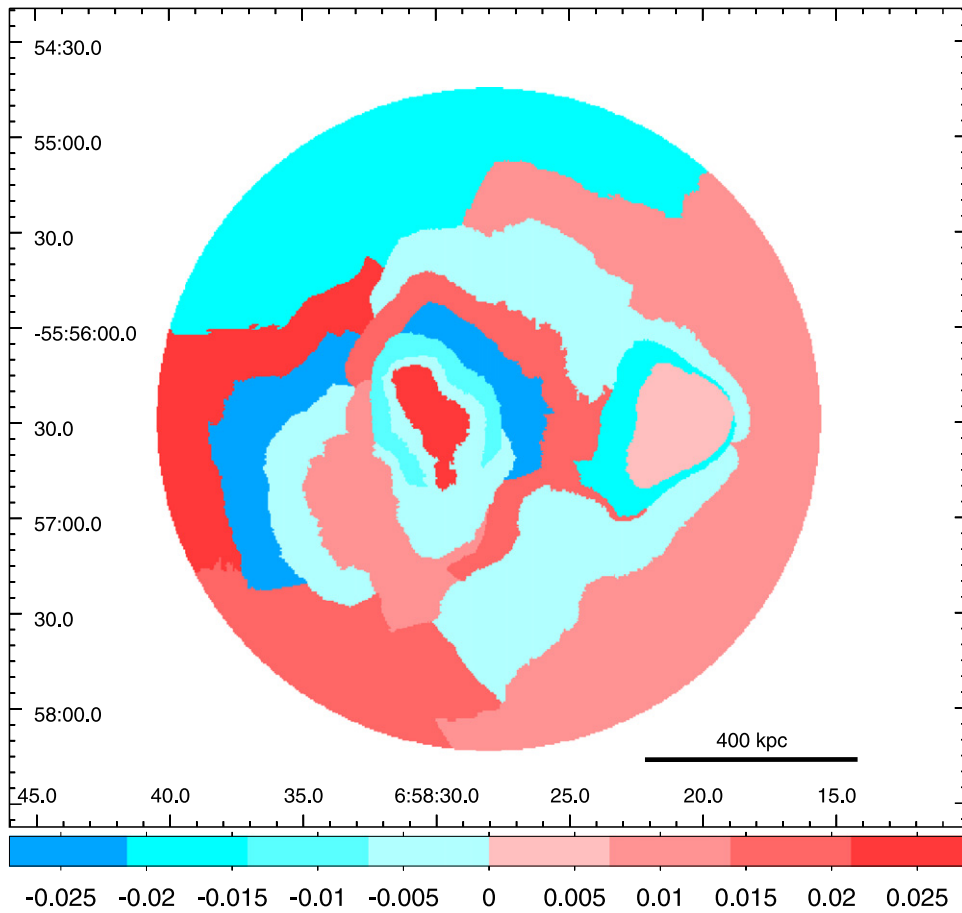


**Figure 5.** Redshift map of the ICM in the Bullet cluster computed with respect to the average redshift  $\langle z_X \rangle = 0.2986$ . The color bar used discrete steps equal to  $\Delta z = 0.007$  which corresponds approximately to the typical  $1\sigma$  error on  $z_X$ .

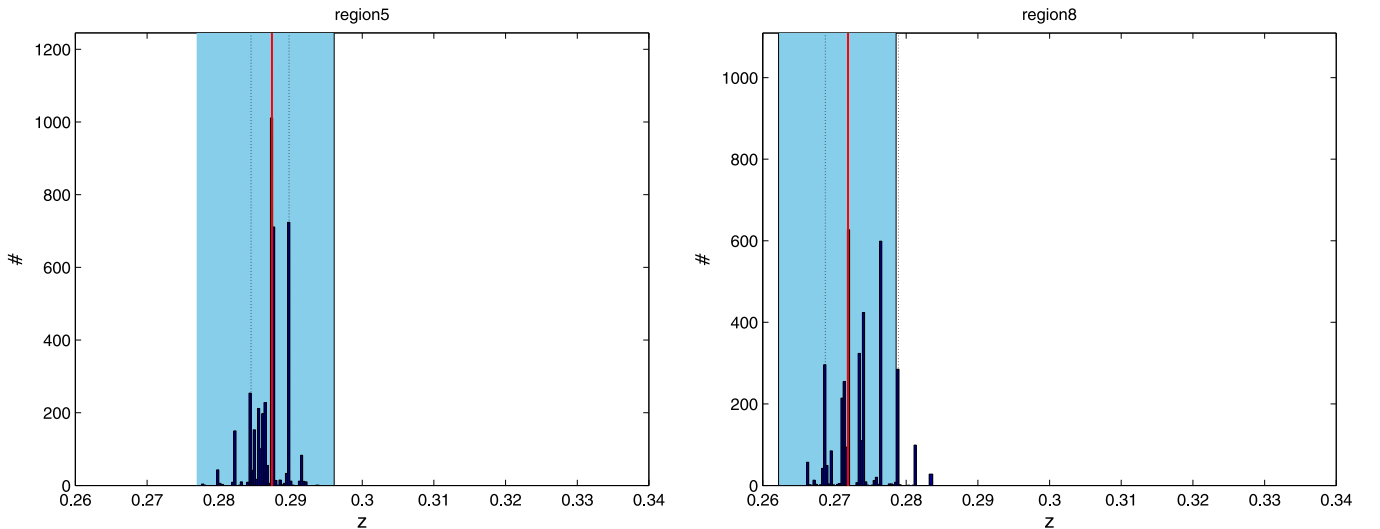


**Figure 6.** Histogram distribution of best-fit  $z_X(T_1, T_2, Z_1, Z_2)$  computed on the subgrid of temperature and abundance values selected as described in the text, for region 5 (left panel) and region 8 (right panel). The central vertical line shows the absolute best-fit  $z_X$ , the dashed area shows the range due to the statistical errors on the absolute best-fit  $z_X$ , and the two vertical dashed lines the lower and upper 90% percentiles of the  $z_X(T_1, T_2, Z_1, Z_2)$  distribution.

the fits performed in the full 0.5–10 keV band, we select the subgrid of  $T_1$ ,  $T_2$ ,  $Z_1$ , and  $Z_2$  values statistically compatible within  $1\sigma$  with the spectrum observed in each region. Then, we again run the spectral fit on the subgrid but in the 2.0–10 keV band only, and measure a set of best-fit  $z_X$  values corresponding to the subgrid parameters. The distribution of  $z_X$  obtained in

this way is used to derive a redshift range defined by the upper and lower 90% percentiles of the  $z_X$  distribution on the grid. Two examples are shown in Figure 6, where the upper and lower 90% percentiles are marked with vertical dashed lines. We remark that the discrete appearance of the distribution is due to the spacing of the parameter grid, since in several cases

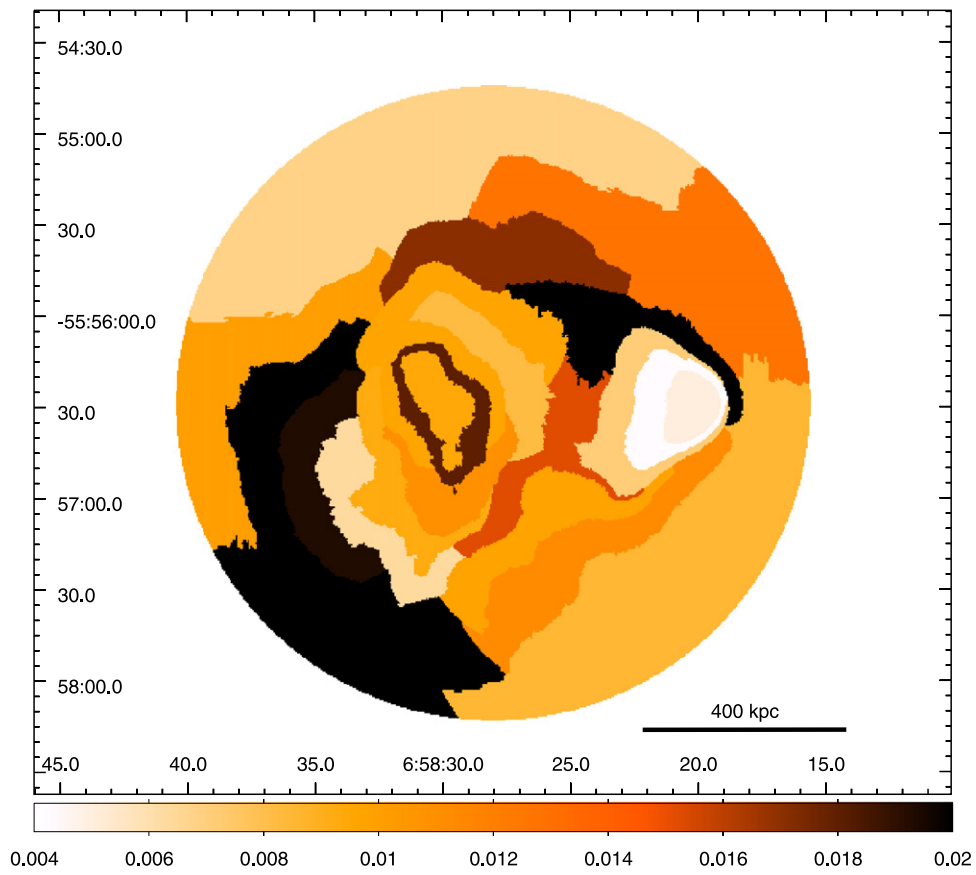


Figure 7. Map of the statistical  $1\sigma$  error on the X-ray redshift  $z_X$ .

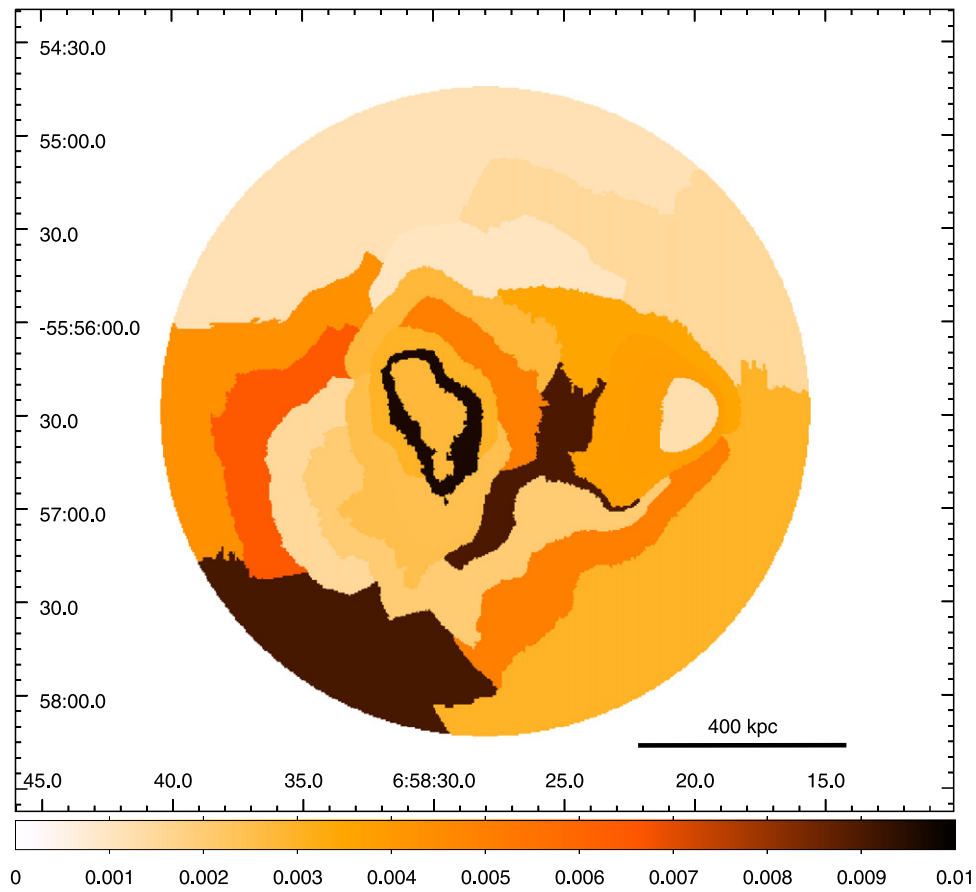
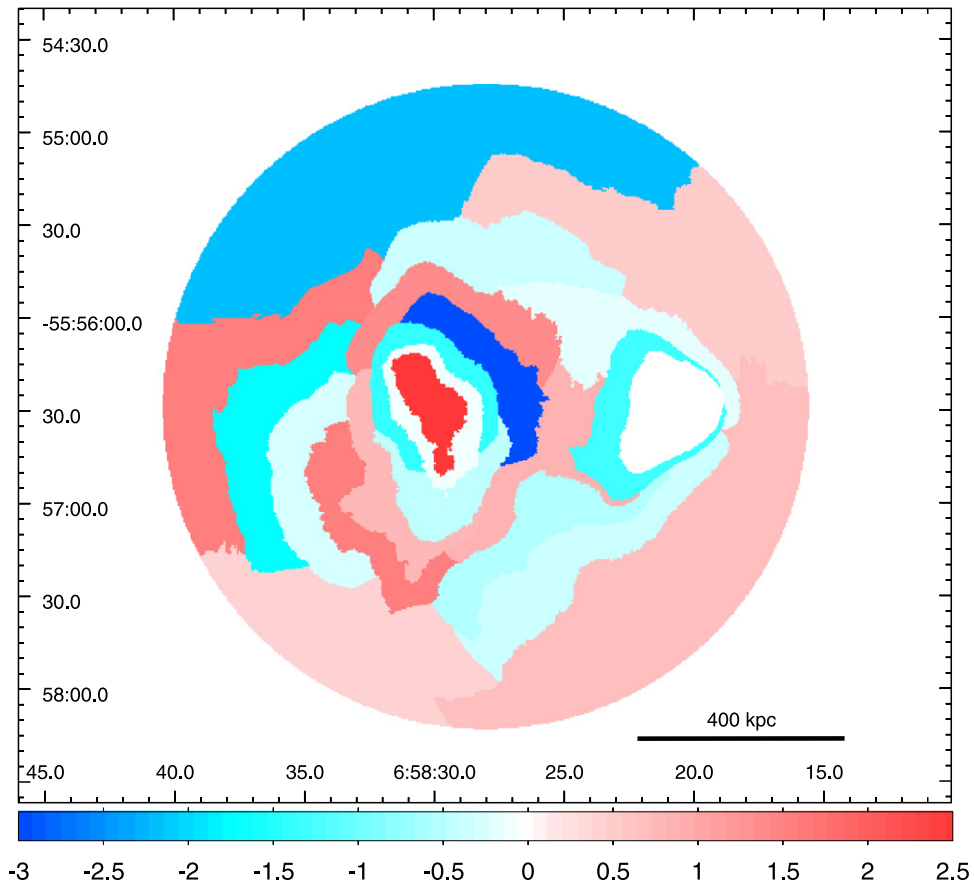


Figure 8. Map of the systematic  $1\sigma$  error on the X-ray redshift  $z_X$ .



**Figure 9.** Significance map obtained as  $(z_X - z_{\text{avg}})/\sigma_{\text{tot}}$ . Only two symmetric regions stand out in bright red and blue colors, while all of the remaining regions have  $z_X$  within less than  $2\sigma$  from  $\langle z_X \rangle$ .

the best-fit redshift is not affected by the metal abundance value. A finer and more time-consuming grid would provide a smoother distribution with little effect, however, on the upper and lower 90% percentiles, as we verified. This range provides an estimate of the systematic uncertainty intervals due to the unknown thermal structure. We remark that the distribution of  $z_X(T_1, T_2, Z_1, Z_2)$  is already broadened by the statistical uncertainty. Therefore, we are confident that the lower and upper 90% percentiles are a conservative upper limit to the real  $1\sigma$  uncertainty due to the thermal structure of the ICM.

We argue that this systematic uncertainty  $\sigma_{\text{syst}}$  is uncorrelated with the statistical error since it is due to the degeneracy of the temperatures values, as discussed in Section 3. Therefore, we estimate the total  $1\sigma$  uncertainty as  $\sigma_{\text{tot}} = \sqrt{\sigma_{\text{stat}}^2 + \sigma_{\text{syst}}^2}$ . The values of  $\sigma_{\text{syst}}$  and  $\sigma_{\text{tot}}$  are shown in Table 5 where we list separately the lower and upper error bars. Although the errors are not symmetric, in Figures 7 and 8, only for the sake of visualization we show a map of the statistical and systematic  $\sigma$  error bars across the cluster image, averaging the lower and upper error bars. The color scale shows the accuracy on  $z_X$ , with brighter regions having smaller errors. It is possible to see that the systematic uncertainties are typically smaller than the statistical ones.

A possible way to combine the information in Figures 5, 7, and 8 is to visualize the significance of the redshift difference as  $(z_X - \langle z_X \rangle)/\sigma_{\text{tot}}$ , which is shown in Figure 9. Here,  $\langle z_X \rangle$  is the average  $z_X$  as computed in Section 5. Bright blue and red regions point out  $\sim 3\sigma$  deviations with respect to the average redshift. It is possible to note that most of the regions are within

$2\sigma$  from  $\langle z_X \rangle$ , while two symmetric regions show a  $3\sigma$  deviation, approximately around the central region of the Bullet cluster. In Figure 10, we show the binned spectra of the two regions with the most extreme redshift (region 1 with  $z_X = 0.3265_{-0.0110}^{+0.0090}$  and region 8 with  $z_X = 0.2719_{0.0102}^{+0.0096}$ ). We focus on the 4.0–7.0 keV energy band to emphasize the difference in the position of the iron line complex in the two regions. In particular, in the right panel of Figure 10, we show the data and best-fit model of region 8 (red solid line and points) along with the best-fit model of region 1 (black solid line). Despite the heavy binning with  $S/N = 9$  per bin, it is possible to visually appreciate the difference in the position of the iron line complex among the two regions. In the following section, we will further investigate and quantify the statistical significance for the presence of bulk motions across the ICM.

## 5. RESULTS ON THE PRESENCE OF BULK MOTIONS

In Figure 11, we show the histogram distribution of the best-fit redshift. The distribution clearly appears as non-Gaussian. However, it is crucial to consider the information on the total error before drawing any conclusions. A direct evaluation of the presence of bulk motion in the ICM of the Bullet cluster is obtained with a simple  $\chi^2$  test of the distribution of  $z_X$ . We consider all of the regions, except for regions 7 and 15, and find  $\chi^2 \equiv \Sigma(z_X - \langle z_X \rangle)^2/\sigma_{\text{tot}}^2 = 32.2$ , which, for 20 degrees of freedom, corresponds to a one-tailed (right-tail) probability value for a  $\chi^2$  test of  $\sim 0.04$ . If we consider the value obtained with our alternative background choice, we find  $\chi^2 = 32.3$ .

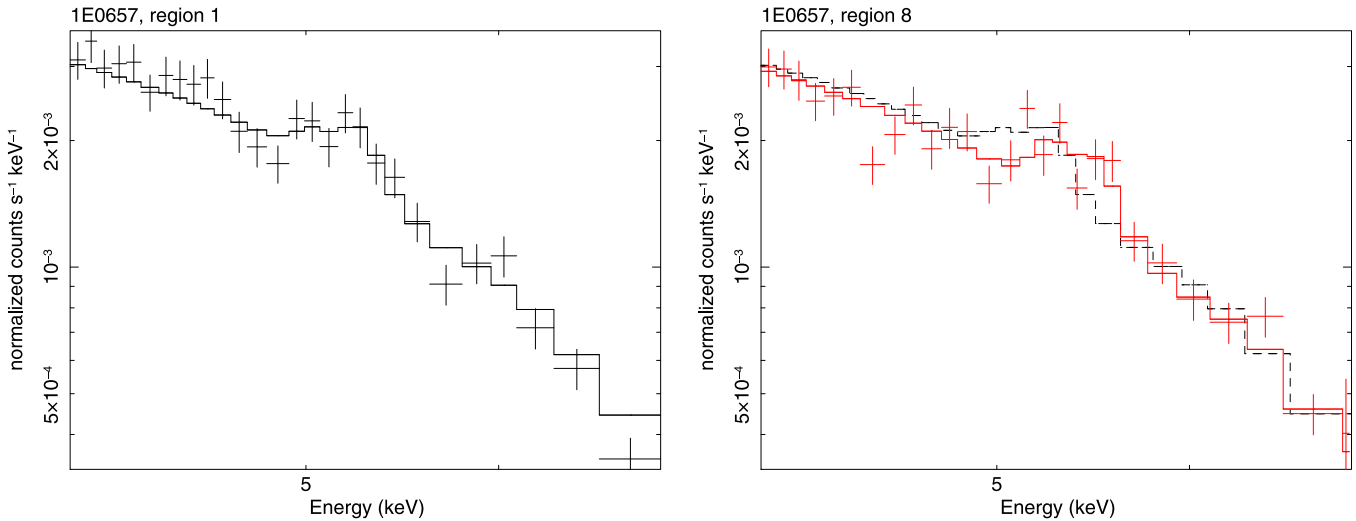


**Figure 10.** Folded spectra of the two regions with the most extreme redshift (left panel: region 1; right panel: region 8). The spectra are binned to a minimum of  $S/N = 9$ , and only the 4.0–7.0 keV energy range is shown. The solid lines show the best-fit model obtained fitting the 2.0–10 keV energy band with two `mekal` components. The dashed line in the right panel shows the best-fit model of region 1.

Therefore, we can conclude that the statistical evidence for inhomogeneities in the overall distribution of  $z_X$  among the ICM regions of the bullet cluster is significant at a  $\sim 2\sigma$  confidence level. Currently, the main limitation we encounter in measuring the bulk motions in the ICM of the Bullet cluster arises due to the statistical error. A better spectral resolution would help to bring this error further below the systematic one, possibly allowing us to confirm the detection of bulk motion obtained in this work. On the other hand, the systematic error can be reduced only by better constraining the high ICM temperatures along the line of sight, which would require a high efficiency, high-resolution, hard X-ray telescope, which is not currently available or planned.

We also search for any possible correspondence between the ICM redshift map and the redshift distribution of the member galaxies. In the SIMBAD astronomical database, we search for galaxies with spectroscopic redshift and within 20 arcmin of the cluster center. We find 108 galaxies meeting these conditions. Then, we fit the distribution of velocities with a Gaussian and perform a  $3\sigma$  clipping by iteratively removing the galaxies whose velocity lies outside  $\pm 3\sigma$  from the mean velocity. We finally identify 80 member galaxies, in agreement with previous works by Barrena et al. (2002) and Guzzo et al. (2009). We compute the mean velocity of the member galaxies as  $\bar{v}_{cl} = 88766 \pm 1252 \text{ km s}^{-1}$  based on the Gaussian best fit, corresponding to an optical redshift of  $z_0 = 0.296 \pm 0.004$ . Both values are consistent with Barrena et al. (2002) and Williamson et al. (2011). We then compute the peculiar velocities of each member galaxy, finding a range from  $-3300 \text{ km s}^{-1}$  to  $3200 \text{ km s}^{-1}$ .

We overplot the member galaxies and their rest-frame velocities on the redshift map (see Figure 12). Each circle with a dot or cross in its center represents a galaxy; the radius of the circle is proportional to the peculiar velocity of the galaxy. Red circles and red crosses stand for member galaxies with positive velocity along the line of sight, while member galaxies with negative velocities are represented by blue circles and blue dots. We do not find any hint of a correlation between the motion of the galaxies and the velocity map of the ICM, suggesting that in any case there are no halos whose galaxies

and ICM move together along the line of sight. We conclude that if there is a significant bulk motion in the ICM, then this is decoupled from the galaxy motions, and therefore is likely to be caused by disordered velocity fields within the ICM generated by the merger event pushing away significant amounts of ICM mass.

To further investigate the direction along the trail of the “bullet,” we select a direction marked in green in Figure 12. In Figure 13, we show the redshift measured in each region crossed along this direction. We note that approximately at the center of the cluster, within the box drawn in Figure 13, the projected redshift of the ICM appears to change significantly within 200–300 kpc, while outside this box the values of  $z_X$  are consistent with the average redshift, shown with a horizontal line. Nominally, the maximum different redshift is  $\Delta z = 0.054 \pm 0.015$ . We can express this results by stating that for a region of  $\sim 200\text{--}300 \text{ kpc}$ , we observe a velocity gradient of  $46 \pm 13 \text{ km s}^{-1} \text{ kpc}^{-1}$ . We argue that this may be the signature of a significant amount of ICM pushed along the line of sight (perpendicularly to the merging) at a velocity of several thousand  $\text{km s}^{-1}$  in both directions.

To summarize, we find marginal evidence of bulk motions in the ICM of the Bullet cluster at a  $2\sigma$  confidence level. If we focus on the bullet path, then we find that the maximum redshift difference is significant at a  $3\sigma$  level between two specific, symmetric regions. If confirmed, then this finding would imply the presence of shocks along the line of sight. We argue that the combination of high-resolution spectroscopy and spatially resolved, moderate resolution spectroscopy may help to resolve the dynamical structure of the ICM in the Bullet cluster.

## 6. EFFECTS OF GAIN CALIBRATION UNCERTAINTIES

So far, we have ignored the effects of the uncertainties in the ACIS-I energy scale calibration (i.e., gain calibration). For example, it is known that there are shifts in the energy of the fluorescent emission lines in the ACIS background due to the change of the detector temperature (see Sanders et al. 2014). To investigate whether this happens in the data of the Bullet cluster, we accurately fit the centroids of the Ni  $K_\alpha$  and Au  $L_\alpha$

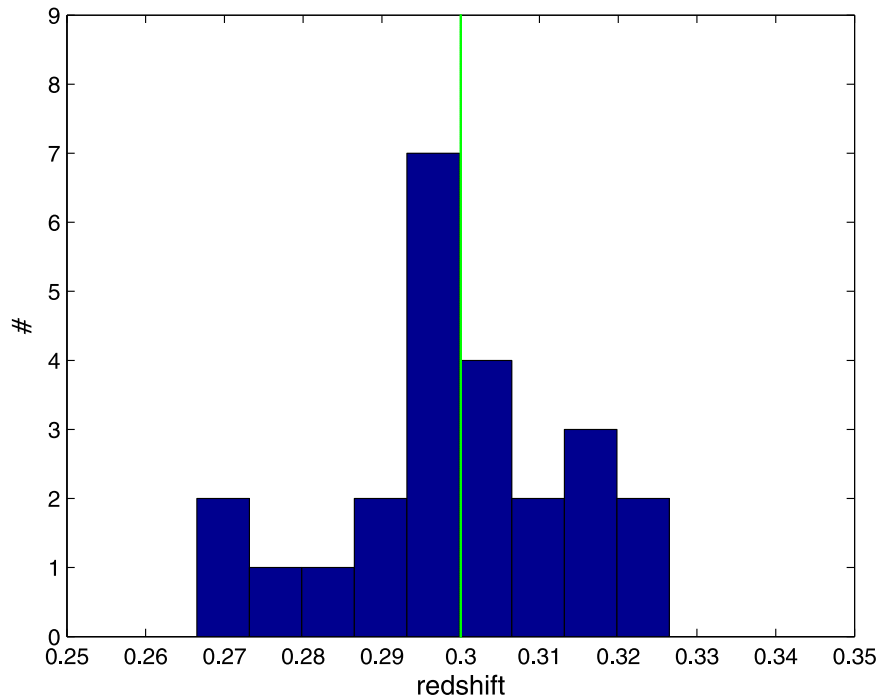


**Figure 11.** Histogram distribution of the best-fit redshift  $z_X$  of the 23 ICM regions. The average redshift  $\langle z_X \rangle = 0.2986$  is shown as a vertical line.

fluorescence lines, which are prominent in the ACIS-I background spectrum at  $\sim 7.5$  and  $\sim 9.7$  keV, respectively. We simply fit in a narrow energy range ( $\sim$  half a keV) a power-law continuum plus a Gaussian line at the position of the two lines. We consider all of the emission from the CCD after excluding a circle of  $104''$  centered on the cluster and all of the point sources. This does not remove all of the cluster emission, but the fluorescence lines strongly dominate the continuum components associated with the ICM emission and the background. The best-fit energies of the two lines in each Obsid are shown in Figure 14. If we consider the statistical error associated with the line energies, then we find that the intrinsic shift in energies between the Obsid is  $\sim 0.010$  keV, which corresponds roughly to  $\Delta z \sim 0.0014$ . This is at least five times smaller than the total uncertainties in  $z_X$ . Therefore, we conclude that the global shift in gain calibration between the nine Obsid does not significantly affect our results and, in any case, should have a mild effect in broadening the iron line profile observed in the total spectrum of each region.

However, we cannot exclude the spatial variation of the gain calibration, which can amplify the fluctuations in the best-fit  $z_X$  values. To estimate the possible bias due to this effect, we again fit the Ni  $K_\alpha$  and Au  $L_\alpha$  fluorescence lines in the spectra of the 23 regions. In this case, the statistical errors associated with the line centroids are much larger, due to the smaller statistics and the much higher contribution from the ICM emission above 7 keV. However, we are able to measure the line centroid for Ni  $K_\alpha$  in most of the regions and for Au  $L_\alpha$  in all of the regions (see Figure 15). The scatter measured among the regions is consistent with statistical noise. A simple  $\chi^2$  test assuming a constant value provides a one-tailed (right-tail) probability value of 0.16 for both lines. This means that there is no evidence for significant gain-calibration variations from region to region that could amplify the  $z_X$  fluctuations found in our analysis. More important, we find that the energy shift we measured, taken at face value (i.e., assuming that the energy

shift is entirely due to an intrinsic change in the gain calibration) typically anticorrelates with the redshift difference we found in our analysis, in particular, in the regions with the largest  $\Delta z$  (regions 8 and 1). If we simply subtract the gain shift map from our  $z_X$  map, then the statistical significance of a deviation from a Gaussian distribution increases. Clearly, we do not consider this correction in our final results, since the gain-fluctuation map is likely to be entirely dominated by the statistical noise.

To summarize, we do not attempt to provide a full treatment of the gain-calibration uncertainties in ACIS-I data, but we perform a direct empirical test which allows us to conclude that any effect associated with gain-calibration uncertainty is safely below the typical statistical errors on our  $z_X$  values, and therefore does not significantly affect our conclusions.

## 7. DISCUSSION

In this work, we developed a method to search for bulk motions in the ICM with *Chandra*, the X-ray facility which is currently providing the best performance in terms of spatially resolved X-ray spectroscopy. Despite this, we are not able to provide definitive evidence for bulk motions along the line of sight in the massive merger cluster 1E 0657-56. We are currently preparing a systematic search of bulk motions in a sample of merging or post-merger clusters observed with *Chandra*, in order to achieve a stronger statistical detection of bulk motions. Currently, we acknowledge that this kind of study is challenging and may provide positive results only in a few extreme cases.

Without any doubt, mapping the velocity field in the ICM in the majority of clusters would be a key tool to studying the process of cluster formation, and to achieving more accurate mass measurements for cosmological studies. Indeed, this is one of the science goals of future planned X-ray missions with micro calorimeters, like the SXS instrument (Mitsuda

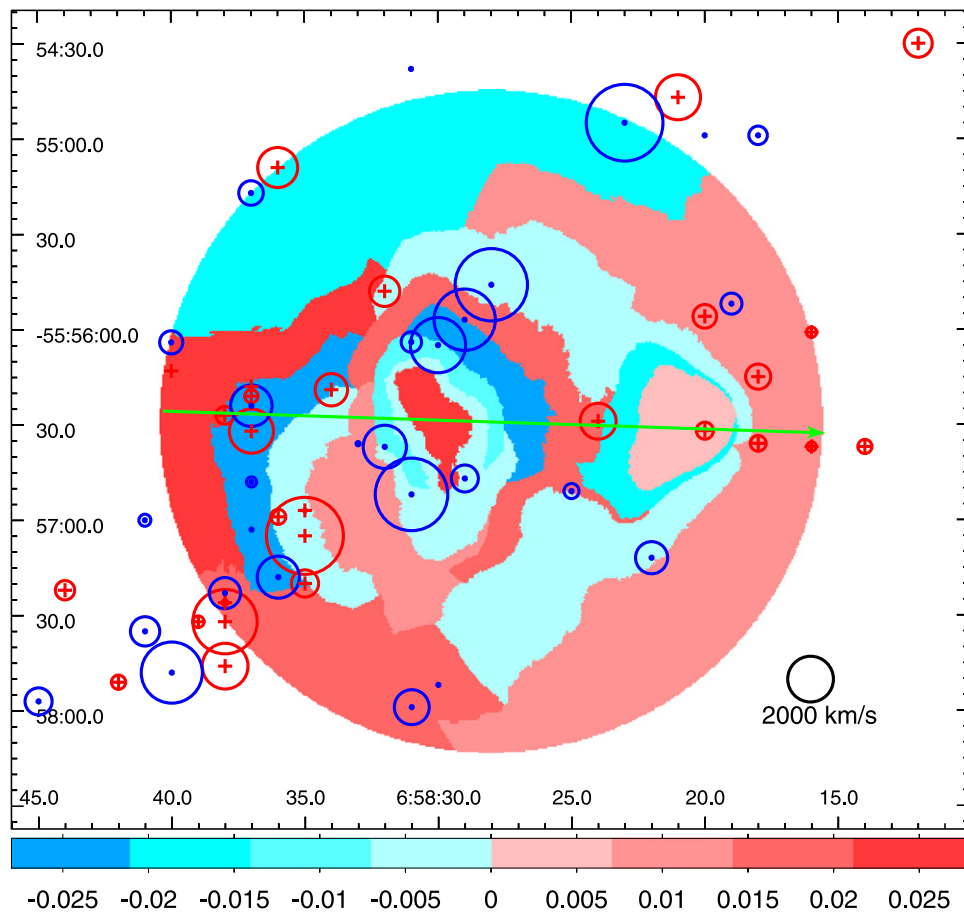


**Figure 12.** Spatial distribution of 80 member galaxies overplotted on the ICM redshift map. The radius of the circles is proportional to the peculiar velocity of the galaxy. Red circles and red crosses stand for member galaxies with  $v_{\text{rest}} > 0$ , while blue circles and blue dots stand for member galaxies with  $v_{\text{rest}} < 0$ . The green arrow shows the directions we consider to explore the X-ray redshift along the bullet trail (see Figure 13).

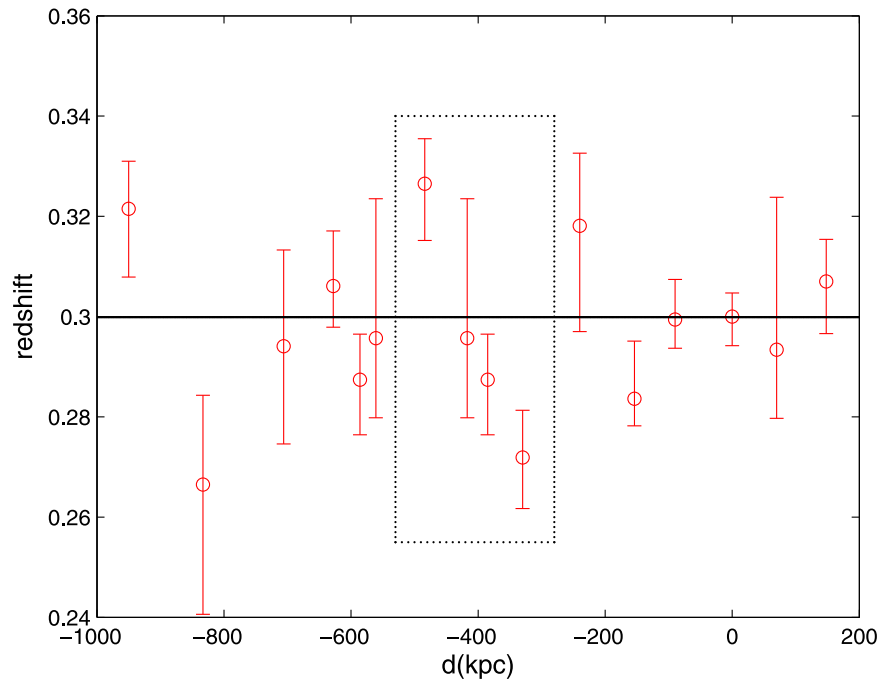


**Figure 13.** Redshift measured along the direction of the bullet where the  $x$ -axis is the distance from the peak of the X-ray brightness (the head of the bullet). The average redshift  $\langle z_x \rangle = 0.2986$  is shown as a horizontal line. The dashed box roughly identifies the region in which we observe a velocity gradient of  $(46 \pm 13)$   $\text{km s}^{-1} \text{kpc}^{-1}$ .

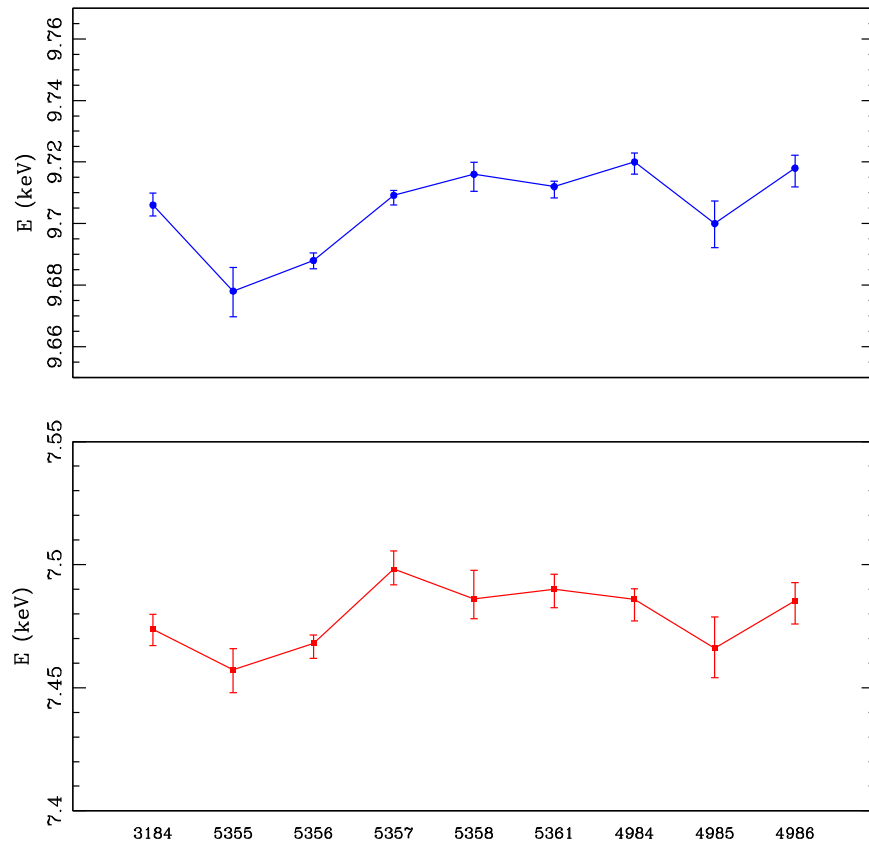


**Figure 14.** Best-fit energies for the fluorescent lines of Au  $L_{\alpha}$  (upper panel) and Ni  $K_{\alpha}$  (lower panel) in each Obsid with corresponding  $1\sigma$  error bars.

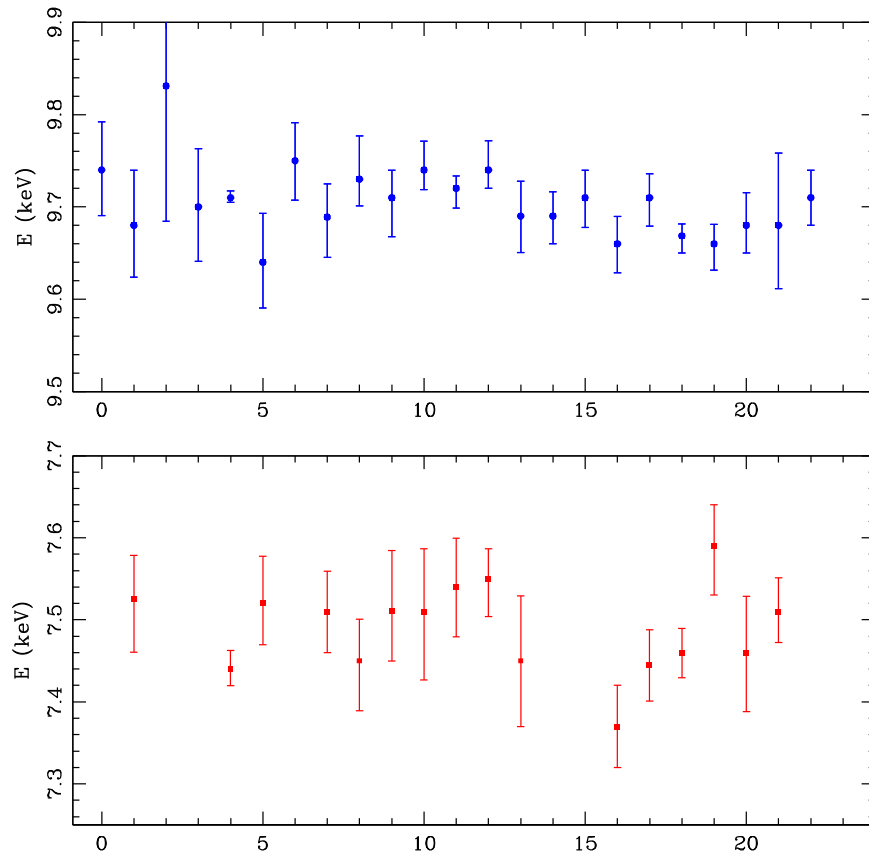


**Figure 15.** Best-fit energies for the fluorescent lines of Au  $L_{\alpha}$  (upper panel) and Ni  $K_{\alpha}$  (lower panel) lines in each region with the corresponding  $1\sigma$  error bars. Note that we are not able to identify the Ni  $K_{\alpha}$  line in several regions, while the Au  $L_{\alpha}$  line is always detected.

et al. 2010) on board *ASTRO-H* (Takahashi et al. 2012), which will also reach the 6.7–6.9 keV energy range corresponding to the rest-frame  $K_{\alpha}$  iron emission lines. With an average spectral resolution of about 7 eV, it is possible to find bulk motions at least in the brightest nearby clusters (see Tamura et al. 2014a). In addition, the line broadening can be measured opening the way to the investigation of ICM turbulence. However, a detailed study requires sophisticated approaches to properly measure the profiles of the emission lines (see, e.g., Shang & Oh 2012) to overcome limitations due to poor angular resolution.

In the future, bulk motion studies will be possible both with CCD and microcalorimeter spectra thanks to the *Athena* mission (Barcons et al. 2012). The much higher effective area with respect to *Chandra* will help to increase significantly the accuracy of the centroid of the iron emission lines. However, the limited spectral resolution of the CCD data will not help to remove the spectral degeneracy among different spectral components, and therefore the angular resolution still remains crucial to analyzing separately regions with different dynamical properties. On the other hand, the X-ray Microcalorimeter Spectrometer on board *Athena* will be able to achieve a redshift accuracy of  $10^{-5}$  in one pointing with an exposure of only 100 ks for a cluster like A2256 (see Nevalainen 2013), which is three orders of magnitude larger than the accuracy achieved in this work. Clearly, the angular resolution will be crucial in order to investigate the 3D dynamical state of clusters, particularly at high redshift where the fraction of major mergers is expected to increase significantly.

X-ray spectroscopy is not the only means to investigate bulk motions in the ICM. In particular, the bulk motion in 1E 0657-56 may also be detected by the kinetic Sunyaev Zeldovich effect (kSZE) caused by the Doppler effect of the cluster radial bulk motion (see Carlstrom et al. 2002). The advent of high-resolution SZE imaging of clusters, reaching the  $10''$ – $30''$  regime, opens a new window on the study of ICM bulk motions. In a few cases, SZE enhancements have been interpreted as effects of the ICM dynamics (see Mason et al. 2010, for the case of RXJ1347). Recent simulations have investigated this aspect, showing that kSZE observations may be effective for probing the ICM motions in major mergers. However, based on our results, the kSZE in the Bullet cluster is expected to appear on scales of  $\sim 4''$ – $5''$ , which requires an angular resolution of at least  $2''$ , which is out of reach for present-day SZ telescopes (Kelley et al. 2010; Barcons et al. 2012). Therefore, the detection of kSZE in the Bullet cluster appears to be challenging despite the strong SZE signal observed using the APEX-SZ instrument at 150 GHz with a resolution of  $1'$  (Halverson et al. 2009). To summarize, the investigation of ICM bulk motions across the majority of the known cluster population will be extremely difficult in the near future, and a major breakthrough in this field may be achieved only with a specially designed instrument.

## 8. CONCLUSIONS

We propose a simple method to search for ICM bulk motions in *Chandra* CCD data, exploiting the high angular resolution to perform spatially resolved X-ray spectroscopy. The method consists of fitting spectra extracted from the ICM region selected on the basis of the surface brightness contours. The fitting model is given by two *mekal* components with all of the parameters set free except the redshift, which is the same

for the two thermal components. The fits are performed on the hard 2.0–10 keV band only to focus on the 6.7–6.9 keV He-like and H-like iron emission lines.

We apply this method to the Bullet cluster 1E 0657-56, a bright, massive merging cluster at  $z \sim 0.3$ . The choice of this cluster for testing our method is based on an expectation of high bulk motions due to the large kinetic energy associated with the merger of two massive clusters. On the other hand, the large temperatures involved,  $kT > 10$  keV, make spectral diagnostics quite difficult for an X-ray instrument like *Chandra* ACIS-I, which has an effective area rapidly decreasing above 7 keV. In order to reach the required accuracy in redshift, we select regions with about  $2 \times 10^4$  photons in the full 0.5–10 keV band, a requirement much stronger than that usually used to measure the X-ray redshift.

We measure  $z_X$  in 23 independent regions, and in each region we accurately evaluate the statistical error on  $z_X$  and the systematic uncertainty associated with the unknown thermal structure of the ICM along the line of sight. This allows us to estimate the total  $1\sigma$  error on  $z_X$ . We find that the distribution of  $z_X$  is inconsistent with a constant redshift across the ICM of the Bullet cluster at the  $2\sigma$  confidence level. If we focus on a particular direction corresponding to the path of the bullet, then we observe a velocity gradient of  $46 \pm 13$  km s $^{-1}$  kpc $^{-1}$  for a region 200–300 kpc in size in the center of the cluster. Finally, we verify a posteriori that uncertainties in the gain calibration do not significantly affect our results.

We argue that this may be due to relevant masses of ICM being pushed away perpendicularly to the direction of the merger in the trail of the bullet. Clearly, at this stage, we cannot discriminate from a full rotation due to an off-center merging from a disordered velocity field. We stress that if confirmed, this will be the detection of true, merger-induced bulk motion in a virialized cluster, at variance with a velocity difference due to a pre-merger stage with two dark matter halos, still carrying their ICM, falling toward each other.

In this work, we push the limits of what is possible with *Chandra*. In addition, the Bullet cluster constitutes a difficult test for our method due to the very high temperatures involved, which make the measurement of the iron emission-line complex much harder than in colder ICM. Despite this, we find interesting hints as to the possible presence of bulk motions in the ICM due to the ongoing merger. Our future plan is to extend this study to a small sample of merging or post-merger clusters to identify the most promising cases where bulk motions can be successfully identified with *Chandra*. Currently, the capability of this analysis is limited due to the low spectral resolution of CCD data. In the future, the systematic measurement of the ICM velocity structure may have a strong impact on cluster physics, helping to reconstruct the assembly process of clusters across cosmic epochs and to derive more accurate total masses for cosmological tests. It would be important to plan future missions able to deliver spatially resolved observations with X-ray micro calorimeters to achieve a major breakthrough in the study of the dynamics of the ICM.

We sincerely thank Craig Gordon and Keith Arnaud for their help and suggestions on the *Xspec* fitting procedure. We also thank the anonymous referee for detailed and in-depth comments which helped to improve this paper. This work was supported by the Ministry of Science and Technology National Basic Science Program (Project 973) under grant

Nos. 2012CB821804 and 2014CB845806, the Strategic Priority Research Program “The Emergence of Cosmological Structure” of the Chinese Academy of Sciences (No. XDB09000000), the National Natural Science Foundation of China under grant Nos. 11373014, 11403002, and 11073005, and the Fundamental Research Funds for the Central Universities and Scientific Research Foundation of Beijing Normal University. P.T. is supported by the Recruitment Program of High-end Foreign Experts and he gratefully acknowledges hospitality of Beijing Normal University.

## REFERENCES

- Angus, G. W., Shan, H. Y., Zhao, H. S., & Famaey, B. 2007, *ApJL*, **654**, L13
- Arnaud, K. A. 1996, in ASP Conf. Ser. 101, *Astronomical Data Analysis Software and Systems V*, ed. G. H. Jacoby & J. Barnes (San Francisco, CA: ASP), 17
- Asplund, M., Grevesse, N., & Sauval, A. J. 2005, in ASP Conf. Ser. 336, *Cosmic Abundances as Records of Stellar Evolution and Nucleosynthesis*, ed. T. G. Barnes, III & F. N. Bash (San Francisco, CA: ASP), 25
- Barcons, X., Barret, D., Decourchelle, A., et al. 2012, arXiv:1207.2745
- Barrena, R., Biviano, A., Ramella, M., Falco, E. E., & Seitz, S. 2002, *A&A*, **386**, 816
- Bradač, M., Clowe, D., Gonzalez, A. H., et al. 2006, *ApJ*, **652**, 937
- Brodwin, M., McDonald, M., Gonzalez, A. H., et al. 2015, arXiv:1504.01397
- Carlstrom, J. E., Holder, G. P., & Reese, E. D. 2002, *ARA&A*, **40**, 643
- Cash, W. 1979, *ApJ*, **228**, 939
- Clowe, D., Bradač, M., Gonzalez, A. H., et al. 2006, *ApJL*, **648**, L109
- Clowe, D., Gonzalez, A., & Markevitch, M. 2004, *ApJ*, **604**, 596
- Clowe, D., Randall, S. W., & Markevitch, M. 2007, *NuPhS*, **173**, 28
- Dupke, R. A., & Bregman, J. N. 2001a, *ApJ*, **562**, 266
- Dupke, R. A., & Bregman, J. N. 2001b, *ApJ*, **547**, 705
- Dupke, R. A., & Bregman, J. N. 2005, *ApJS*, **161**, 224
- Dupke, R. A., & Bregman, J. N. 2006, *ApJ*, **639**, 781
- Dupke, R. A., Mirabal, N., Bregman, J. N., & Evrard, A. E. 2007, *ApJ*, **668**, 781
- Durret, F., Lima Neto, G. B., & Forman, W. 2005, *A&A*, **432**, 809
- Guzzo, L., Schuecker, P., Böhringer, H., et al. 2009, *A&A*, **499**, 357
- Halverson, N. W., Lanting, T., Ade, P. A. R., et al. 2009, *ApJ*, **701**, 42
- Kaastra, J. 1992, *An X-Ray Spectral Code for Optically Thin Plasmas* (Internal SRONLeiden Report, updated version 2.0)
- Kalberla, P. M. W., Burton, W. B., Hartmann, D., et al. 2005, *A&A*, **440**, 775
- Kelley, R. L., Mitsuda, K., Awaki, H., et al. 2010, *BAAS*, **41**, 738
- Komatsu, E., Smith, K. M., Dunkley, J., et al. 2011, *ApJS*, **192**, 18
- Liedahl, D. A., Osterheld, A. L., & Goldstein, W. H. 1995, *ApJL*, **438**, L115
- Liu, T., Tozzi, P., Tundo, E., et al. 2015, *ApJS*, **216**, 28
- Markevitch, M., Gonzalez, A. H., Clowe, D., et al. 2004, *ApJ*, **606**, 819
- Markevitch, M., Gonzalez, A. H., David, L., et al. 2002, *ApJL*, **567**, L27
- Markevitch, M., Randall, S., Clowe, D., Gonzalez, A., & Bradac, M. 2006, in 36th COSPAR Scientific Assembly, Meeting Abstract from CDRM, 2655
- Markevitch, M., & Vikhlinin, A. 2007, *PhR*, **443**, 1
- Mason, B. S., Dicker, S. R., Korngut, P. M., et al. 2010, *ApJ*, **716**, 739
- Mazzotta, P., Rasia, E., Moscardini, L., & Tormen, G. 2004, *MNRAS*, **354**, 10
- Mewe, R., Gronenschild, E. H. B. M., & van den Oord, G. H. J. 1985, *A&AS*, **62**, 197
- Mewe, R., Lemen, J. R., & van den Oord, G. H. J. 1986, *A&AS*, **65**, 511
- Million, E. T., & Allen, S. W. 2009, *MNRAS*, **399**, 1307
- Mitchell, R. J., Culhane, J. L., Davison, P. J. N., & Ives, J. C. 1976, *MNRAS*, **175**, 29P
- Mitsuda, K., Kelley, R. L., Boyce, K. R., et al. 2010, *Proc. SPIE*, **7732**, 11
- Nagai, D., Lau, E. T., Avestruz, C., Nelson, K., & Rudd, D. H. 2013, *ApJ*, **777**, 137
- Nevalainen, J. 2013, *AN*, **334**, 321
- Nousek, J. A., & Shue, D. R. 1989, *ApJ*, **342**, 1207
- Ota, N., Fukazawa, Y., Fabian, A. C., et al. 2007, *PASJ*, **59**, 351
- Press, W. H., Teukolsky, S. A., Vetterling, W. T., & Flannery, B. P. 2002, *Numerical Recipes in C++ : The Art of Scientific Computing* (Baltimore, MD: STScI)
- Rosati, P., Tozzi, P., Ettori, S., et al. 2004, *AJ*, **127**, 230
- Rosati, P., Tozzi, P., Gobat, R., et al. 2009, *A&A*, **508**, 583
- Sanders, J. S. 2006, *MNRAS*, **371**, 829
- Sanders, J. S., Fabian, A. C., Sun, M., et al. 2014, *MNRAS*, **439**, 1182
- Sato, K., Matsushita, K., Ishisaki, Y., et al. 2008, *PASJ*, **60**, 333
- Sato, T., Matsushita, K., Ota, N., et al. 2011, *PASJ*, **63**, 991
- Shang, C., & Oh, S. P. 2012, *MNRAS*, **426**, 3435
- Stanford, S. A., Eisenhardt, P. R., Brodwin, M., et al. 2005, *ApJL*, **634**, L129
- Sugawara, C., Takizawa, M., & Nakazawa, K. 2009, *PASJ*, **61**, 1293
- Takahashi, T., Mitsuda, K., Kelley, R., et al. 2012, *Proc. SPIE*, **8443**, 1
- Tamura, T., Hayashida, K., & Takizawa, M. 2014a, in *Suzaku-MAXI 2014: Expanding the Frontiers of the X-ray Universe*, ed. M. Ishida, R. Petre & K. Mitsuda, 388
- Tamura, T., Hayashida, K., Ueda, S., & Nagai, M. 2011, *PASJ*, **63**, 1009
- Tamura, T., Yamasaki, N. Y., Iizuka, R., et al. 2014b, *ApJ*, **782**, 38
- Tozzi, P., Moretti, A., Tundo, E., et al. 2014, *A&A*, **567**, A89
- Tozzi, P., Santos, J. S., Jee, M. J., et al. 2015, *ApJ*, **799**, 93
- Tozzi, P., Santos, J. S., Nonino, M., et al. 2013, *A&A*, **551**, A45
- Tucker, W., Blanco, P., Rappoport, S., et al. 1998, *ApJL*, **496**, L5
- Tundo, E., Moretti, A., Tozzi, P., et al. 2012, *A&A*, **547**, A57
- Williamson, R., Benson, B. A., High, F. W., et al. 2011, *ApJ*, **738**, 139
- Wilms, J., Allen, A., & McCray, R. 2000, *ApJ*, **542**, 914
- Yu, H., Tozzi, P., Borgani, S., Rosati, P., & Zhu, Z.-H. 2011, *A&A*, **529**, A65